

Fast Estimation of Gravitational and Primordial Bispectra in Large Scale Structures

M.M. Schmittfull¹, D.M. Regan², and E.P.S. Shellard¹

¹*Centre for Theoretical Cosmology, DAMTP, University of Cambridge, CB3 0WA, UK*

²*Department of Physics and Astronomy, University of Sussex, Brighton, BN1 9QH, UK*

(Dated: September 17, 2018)

We present the implementation of a fast estimator for the full dark matter bispectrum of a three-dimensional particle distribution relying on a separable modal expansion of the bispectrum. The computational cost of accurate bispectrum estimation is negligible relative to simulation evolution, so the isotropic bispectrum can be used as a standard diagnostic whenever the power spectrum is evaluated. As an application we measure the evolution of gravitational and primordial dark matter bispectra in N -body simulations with Gaussian and non-Gaussian initial conditions of the local, equilateral, orthogonal and flattened shape. The results are compared to theoretical models using a 3D visualisation, 3D shape correlations and the cumulative bispectrum signal-to-noise, all of which can be evaluated extremely quickly. Our measured bispectra are determined by $\mathcal{O}(50)$ coefficients, which can be used as fitting formulae in the nonlinear regime and for non-Gaussian initial conditions. In the nonlinear regime with $k < 2h \text{ Mpc}^{-1}$, we find an excellent correlation between the measured dark matter bispectrum and a simple model based on a ‘constant’ bispectrum plus a (nonlinear) tree-level gravitational bispectrum. In the same range for non-Gaussian simulations, we find an excellent correlation between the measured additional bispectrum and a constant model plus a (nonlinear) tree-level primordial bispectrum. We demonstrate that the constant contribution to the non-Gaussian bispectrum can be understood as a time-shift of the constant mode in the gravitational bispectrum, which is motivated by the one-halo model. The final amplitude of this extra non-Gaussian constant contribution is directly related to the initial amplitude of the constant mode in the primordial bispectrum. We also comment on the effects of regular grid and glass initial conditions on the bispectrum.

CONTENTS

		Comparison to other bispectrum estimators	13
		Bispectrum visualisation	14
I. Introduction	2		
II. The Distribution of Matter	3	V. Simulation Setup, Initial Conditions and Validation	15
Power spectrum and transfer functions	3	N -body simulations setup	15
Matter bispectrum	3	Regular grid vs glass initial conditions	15
Tree-level gravitational matter bispectrum	3	Validation and convergence tests	16
Gravitational matter bispectrum beyond tree level	4	Error bars	17
Loop corrections	4		
Halo models	5	VI. Gravitational Bispectrum Results	18
Constant ‘halo’ model	6	Gravitational collapse and bispectrum evolution	18
Alternative phenomenological fit	6	Comparison with leading order PT	18
III. Primordial Non-Gaussianity	7	Fitting formulae for Gaussian simulations	19
Primordial contribution to the matter bispectrum	7	Separable polynomial expansion	19
Non-Gaussianity as a halo model time-shift	7	Time-shift model fit	21
Primordial bispectrum shapes from inflation	9	Alternative phenomenological fit	25
Local shape	9	Halo model	26
Equilateral shape	9	VII. Primordial Non-Gaussian Bispectrum Results	26
Orthogonal shape	10	Primordial bispectrum measurements	26
Flattened shape	10	Local shape	26
IV. Bispectrum Estimation Methodology	10	Other shapes	26
f_{NL} estimator	10	Loop corrections for primordial non-Gaussianity	28
Shape and size comparisons	11	Linearity in input f_{NL}	28
Separable mode expansion for fast f_{NL} estimation	11	Fitting formulae for non-Gaussian simulations	28
Fast modal bispectrum estimator	12	Separable polynomial fits	28
Fast modal bispectrum correlations	13	Time-shift model fits	28
Cumulative measures of non-Gaussianity	13	Redshift at which 1-halo contribution becomes important	32
Towards experimental setups	13		

VIII. Summary and Conclusions	32
Acknowledgements	33
References	33

I. INTRODUCTION

Observations of the cosmic microwave background (CMB) [1–4] and large scale structure (LSS) [5, 6] are currently consistent with Gaussian primordial cosmological perturbations. Much effort has been undertaken in recent times to constrain a possible non-Gaussian contribution. Detection of a significant primordial bispectrum or trispectrum would have major implications for the mechanism of inflation, possibly ruling out the simplest paradigm of canonical single-field slow-roll inflation. Given this possibility, the importance of developing methods that discriminate between the plethora of inflationary models is clear. Such general methods have been developed in the case of the CMB in [2, 4, 7–9]. This work exploited the use of a separable expansion of the underlying bispectrum or trispectrum in order to greatly reduce the computational cost involved in analysing general shapes.

The CMB bispectrum is currently the most powerful and direct probe of primordial non-Gaussianity, and higher resolution temperature and polarisation data will soon be available from Planck. Nevertheless, interest in the possibility of using observables of large scale structure to test primordial non-Gaussianity has undergone a recent resurgence, due in part to the potentially three dimensional nature of the dataset as a result of its redshift dependence. In particular, the scale-dependent bias induced by non-Gaussian local initial conditions on the halo power spectrum has been shown in [10] to offer an additional and powerful probe. Much work has been undertaken to improve analytic predictions for the impact of non-Gaussian initial conditions on the matter and galaxy power spectrum and bispectrum (see for example [11–21] and references therein). In [6, 22] constraints on local-type non-Gaussianity were found at levels competitive with those obtained using CMB data. Despite these advances it is notable that until recently only local type non-Gaussianity had been studied using large-scale structure, owing to the difficulty in generating generic initial conditions. This situation greatly improved due to work by Wagner and Verde [23, 24] and work by Scoccimarro et al. [25]. However, both of these approaches become inefficient for non-separable bispectra. In [26] the possibility of using the separable expansion method, exploited to great effect in the case of the CMB [2], was explored. This approach was verified in [27] to allow for a far more efficient generation of non-Gaussian initial conditions than had previously been possible in the literature. Further-

more, the separable decomposition methodology allows for the study of non-separable shapes. This has allowed for a robust and truly general approach towards the generation of primordial non-Gaussian initial conditions for use in N -body simulations. In this paper we exploit this approach to set up and run N -body simulations with non-Gaussian initial conditions. In particular, we study initial conditions given by local, equilateral, orthogonal and flattened bispectra, respectively. We choose the flattened (or trans-Planckian) model as an explicit example of an inherently non-separable bispectrum. We exploit the modal method to efficiently and accurately reconstruct the full 3D matter bispectrum at each redshift of interest for each of these non-Gaussian models. This allows us to correlate the results of the N -body simulations with analytic estimates, allowing us to identify clearly the regime at which nonlinear corrections become important. This applies first to accurately determining the gravitational bispectrum well into the nonlinear regime, which is necessary in order to differentiate the more subtle impact of primordial non-Gaussianity. The correlation measure proves useful in distinguishing the different primordial shapes. We also thoroughly test the impact of starting N -body simulations using either glass or regular grid initial conditions. We emphasise that our purpose here is to study the detailed nature of the underlying matter bispectrum derived from N -body simulations. These methods can be equally applied to efficiently extract the galaxy bispectrum from huge survey data sets or to predict the halo bispectrum from simulations in a realistic observational context, but this will be the subject of future work.

The paper is organised as follows. In Section II we review the generation of non-Gaussianity due to nonlinear gravitational evolution, together with the physically-motivated models we will use to describe our results. In Section III we review primordial non-Gaussianity, introduce the specific models studied in this paper and discuss their impact on the matter bispectrum, proposing a new time-shift model. In Section IV we discuss the bispectrum estimation methodology based on a separable expansion which allows extremely efficient estimation of the full N -body bispectrum, as well as the cumulative signal-to-noise and its correlation to theoretically-predicted bispectra. We discuss the simulation setup, impact of glass initial conditions, validations and convergence tests in Section V. In Section VI we present our results for the gravitational bispectrum and the simple fits thereof, while primordial bispectra in non-Gaussian simulations and their fits are discussed in section VII. Finally, in Section VIII we present our conclusions. Readers familiar with the modal methodology and interested primarily in the measured bispectra and testing of various fitting formulae may wish to start with Section VI and follow the references to the earlier sections given there.

II. THE DISTRIBUTION OF MATTER

Power spectrum and transfer functions

The distribution of matter in the universe can be described by its fractional overdensity $\delta(\mathbf{x}) = (\rho(\mathbf{x}) - \bar{\rho})/\bar{\rho}$, where $\bar{\rho}$ is the spatial average of the density $\rho(\mathbf{x})$. An important prediction of cosmological models is the probability of finding a certain configuration $\delta(\mathbf{x})$ in the universe. The simplest possibility is a Gaussian pdf, which is determined by the two-point correlation function, or in Fourier space by the power spectrum P_δ ,

$$\langle \delta(\mathbf{k}_1)\delta(\mathbf{k}_2) \rangle = (2\pi)^3 \delta_D(\mathbf{k}_1 + \mathbf{k}_2) P_\delta(k_1). \quad (1)$$

Here we assumed statistical homogeneity, leading to the Dirac delta function, and statistical isotropy, which implies that the power spectrum only depends on the magnitude of the wavevector.

Perturbations from inflation are usually described by the comoving curvature perturbation \mathcal{R} , which is related to the primordial potential Φ by $\Phi = -3\mathcal{R}/5$, in linear perturbation theory during matter domination. The density perturbation δ can be obtained using the linear Poisson equation

$$\delta(\mathbf{k}, z) = \frac{2}{3} \frac{k^2 T(k) D(z)}{\Omega_m H_0^2} \Phi(\mathbf{k}) \equiv M(k, z) \Phi(\mathbf{k}), \quad (2)$$

where $T(k)$ is the linear transfer function at low redshift normalised to $T(k) = 1$ on large scales and calculable with CAMB [28], and $D(z)$ is the linear growth function for $\Omega_{\text{rad}} = 0$ [29] normalised to $D(z) = 1/(1+z)$ during matter domination. Later we will also find it convenient to use the growth function normalised to unity today, $\bar{D}(z) = D(z)/D(0)$.

At late times and on small scales, the linear treatment breaks down and N -body simulations must be used to find the nonlinear transfer of primordial to late time perturbations. A widely used fit of the nonlinear power spectrum is HALOFIT [30], which is included in CAMB [28]. However, in our own bispectrum analysis we will generally use the actual nonlinear power spectrum measured from the N -body simulations.

Matter bispectrum

At late times, the model of a Gaussian pdf for the density perturbation is over-simplified because nonlinear gravitational collapse will lead to higher order correlations. To study deviations from Gaussianity, it is useful to consider the *bispectrum* B_δ (or three-point correlator transform), which is defined by

$$\langle \delta(\mathbf{k}_1)\delta(\mathbf{k}_2)\delta(\mathbf{k}_3) \rangle = (2\pi)^3 \delta_D(\Sigma_i \mathbf{k}_i) B_\delta(k_1, k_2, k_3), \quad (3)$$

assuming again statistical homogeneity and isotropy. The Dirac delta function imposes a triangle constraint on the bispectrum arguments k_1, k_2, k_3 . The space of triangle configurations is sometimes called a tetrapyd [8] and is shown in Fig. 1. Additionally to the triangle constraint, we impose a cut off at k_{max} , corresponding to the smallest scale under consideration. The bispectrum shape, i.e. its dependence on the wavenumbers k_i , gives important information about the physics which induced the bispectrum. Not only does it help to disentangle late time non-Gaussianity, e.g. induced by nonlinear gravitational collapse, from primordial inflationary non-Gaussianity, but it also opens the intriguing possibility of distinguishing between different inflationary models. To see this explicitly we will review the perturbative treatment of such non-Gaussianities in the following sections.

Tree-level gravitational matter bispectrum

The equations of motion for a perfect pressureless fluid in a homogeneous and isotropic universe contain nonlinearities, which induce a non-vanishing bispectrum (see e.g. [31, 32] for details). Specifically these are the $\nabla \cdot (\delta \mathbf{v})$ term in the continuity equation and the $(\mathbf{v} \cdot \nabla) \mathbf{v}$ term in the Euler equation, where \mathbf{v} is the peculiar velocity, which describes deviations from the background Hubble flow. To see how these terms induce a non-Gaussian density perturbation one makes a perturbative ansatz for the density perturbation (see [31] for a review)

$$\delta(\mathbf{k}, t) = \sum_{n=1}^{\infty} a(t)^n \delta_n(\mathbf{k}) \quad (4)$$

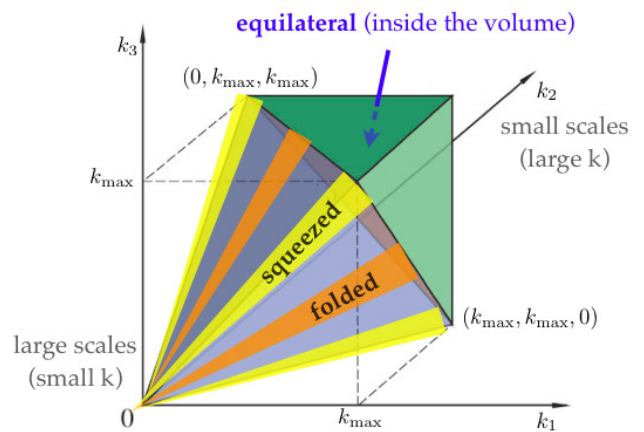


Figure 1. Space of triangles with sides k_1, k_2, k_3 , i.e. each point inside the tetrapyd volume corresponds to a triangle configuration. Squeezed, folded and equilateral configurations are highlighted.

and similarly for the peculiar velocity, which is assumed to be described completely by its divergence, $\theta \equiv \nabla \cdot \mathbf{v}$. Then the equations of motion imply (see [31] and references therein)

$$\delta_n(\mathbf{k}) = \int d^3\mathbf{q}_1 \cdots \int d^3\mathbf{q}_n \delta_D(\mathbf{k} - \mathbf{q}_1 - \cdots - \mathbf{q}_n) F_n^{(s)}(\mathbf{q}_1, \dots, \mathbf{q}_n) \delta_1(\mathbf{q}_1) \cdots \delta_1(\mathbf{q}_n), \quad (5)$$

and determine the kernels $F_n^{(s)}$, e.g.

$$F_2^{(s)}(\mathbf{k}_1, \mathbf{k}_2) = \frac{5}{7} + \frac{1}{2} \frac{\mathbf{k}_1 \cdot \mathbf{k}_2}{k_1 k_2} \left(\frac{k_1}{k_2} + \frac{k_2}{k_1} \right) + \frac{2}{7} \left(\frac{\mathbf{k}_1 \cdot \mathbf{k}_2}{k_1 k_2} \right)^2. \quad (6)$$

Here the first and second terms come, respectively, from $\delta \nabla \cdot \mathbf{v}$ and $\mathbf{v} \cdot \nabla \delta$ in the continuity equation, while the last term comes from $(\mathbf{v} \cdot \nabla) \mathbf{v}$ in Euler's equation [32].

At high redshift, the expansion (4) is dominated by δ_1 and $\delta_2 \sim F_2^{(s)} \delta_1^2$. If we assume δ_1 to be Gaussian, the leading order contribution to the gravitational bispectrum is given by [33]

$$B_\delta^{\text{grav}}(k_1, k_2, k_3) = 2P_\delta^L(k_1)P_\delta^L(k_2)F_2^{(s)}(\mathbf{k}_1, \mathbf{k}_2) + 2 \text{ perms}, \quad (7)$$

where P_δ^L is the power spectrum of the linear perturbation δ_1 .

To discuss the shape of this gravitational bispectrum let us consider two-dimensional slices through the tetrapyd shown in Fig. 1, with $k_1 + k_2 + k_3 = \text{const.}$ We denote one side of these two-dimensional triangular slices as α and parameterise the other direction with β .¹ A slice through the gravitational bispectrum (7) is shown in Fig. 2a (see [34] for more slices at slightly different length scales). The bispectrum is maximal at the edges of the plot, corresponding to flattened triangle configurations, where $k_1 + k_2 = k_3$ or permutations thereof, i.e. where the wavevectors \mathbf{k}_i are parallel or anti-parallel to each other. However there is a suppression in the corners of the plot, corresponding to squeezed triangle configurations with $k_1 \ll k_2 \approx k_3$ or permutations thereof. Non-flattened and equilateral triangle configurations in the centre of the plot are also suppressed. This tree level gravitational bispectrum is also illustrated in Fig. 3 as a function over the full tetrapyd.

To understand the basic shape of the gravitational bispectrum (7) we plot in Fig. 2b the expression $2P_\delta^L(k_1)P_\delta^L(k_2) + 2 \text{ perms}$, which corresponds to replacing $F_2^{(s)}$ in (7) by a constant. Comparing Fig. 2b with Fig. 2a shows that the configuration dependence of the

kernel (6), which is induced by the terms containing scalar products, leads to an enhancement of flattened and particularly folded configurations, where two of the wavevectors \mathbf{k}_i equal each other. Non-flattened configurations are relatively suppressed. As we go along the edge of the plot in Fig. 2a, from folded ($k_1 = k_2 = k_3/2$ or permutations) to squeezed configurations ($k_1 \ll k_2 \approx k_3$ or permutations), the bispectrum shape reflects the shape of the power spectrum P_δ^L , which peaks at $k_{\text{eq}} \approx 0.02h/\text{Mpc}$ and then decreases with decreasing k_1 because $P_\delta^L(k_1) \propto k_1$ on large scales.

Further discussion is required in the squeezed limit, where $\mathbf{k}_2 \approx -\mathbf{k}_3$. Let us consider the regime where $k_1 < k_{\text{eq}}$ and $k_2, k_3 > k_{\text{eq}}$. The term with $P_\delta^L(k_2)P_\delta^L(k_3)$ in (7) is small since the small scale power spectra decrease rapidly with increasing k_2, k_3 and $F_2^{(s)}(\mathbf{k}_2, \mathbf{k}_3)$ vanishes for $\mathbf{k}_2 = -\mathbf{k}_3$. The other two permutations in (7) depend on the angle between the large-scale wavevector \mathbf{k}_1 and the small-scale wavevectors $\mathbf{k}_2, \mathbf{k}_3$. First consider the case where the large scale is approximately perpendicular to the two small scales, i.e. $\mathbf{k}_1 \cdot \mathbf{k}_2 \approx -\mathbf{k}_1 \cdot \mathbf{k}_3 \approx 0$. Then $F_2^{(s)}(\mathbf{k}_1, \mathbf{k}_2) \approx F_2^{(s)}(\mathbf{k}_1, \mathbf{k}_3) \approx 5/7$ and $P_\delta^L(k_1)P_\delta^L(k_2)$ and $P_\delta^L(k_1)P_\delta^L(k_3)$ decrease as we approach more squeezed triangles, implying a suppressed bispectrum in the squeezed limit. In the other limit, the large-scale wavevector \mathbf{k}_1 is not orthogonal to the small scale wavevectors, and so is aligned with one or other of $\mathbf{k}_2, \mathbf{k}_3$. Then the squeezed limit $k_1 \rightarrow 0$ implies $F_2^{(s)}(\mathbf{k}_1, \mathbf{k}_2) \propto k_1^{-1} \rightarrow \infty$ and $F_2^{(s)}(\mathbf{k}_1, \mathbf{k}_3) \propto -k_1^{-1} \rightarrow -\infty$, which can be seen in Fig. 2c. However, in the sum

$$P_\delta^L(k_1)P_\delta^L(k_2)F_2^{(s)}(\mathbf{k}_1, \mathbf{k}_2) + P_\delta^L(k_1)P_\delta^L(k_3)F_2^{(s)}(\mathbf{k}_1, \mathbf{k}_3),$$

the two terms containing k_1^{-1} divergences in the kernel approximately cancel, because $k_2 \approx k_3$ and $\mathbf{k}_1 \cdot \mathbf{k}_2 \approx -\mathbf{k}_1 \cdot \mathbf{k}_3$. Also in the limit $k_1 \rightarrow 0$, the divergences of the kernels are regulated by the large scale power spectrum because $k_1^{-1}P_\delta^L(k_1) = \text{const.}$ on very large scales. Fig. 2a shows that the divergences are indeed cancelled in the total bispectrum (7) and the squeezed limit is suppressed if the large-scale wavenumber satisfies $k_1 < k_{\text{eq}}$.

Gravitational matter bispectrum beyond tree level

Loop corrections

The tree level prediction for the gravitational matter bispectrum (7) is only a good approximation on large scales and can be improved by including so-called loop corrections, which were derived for Gaussian initial conditions in [32] and extended to include non-Gaussian initial conditions in [11]. Important loop corrections can be included simply by replacing the linear power spectrum P_δ^L by the nonlinear power spectrum P_δ in the tree level

¹ Details can be found in [7]. The slice parameters α, β should not be confused with the expansion coefficients $\alpha_n^{\{Q,R\}}$ and $\beta_n^{\{Q,R\}}$ to be defined later.

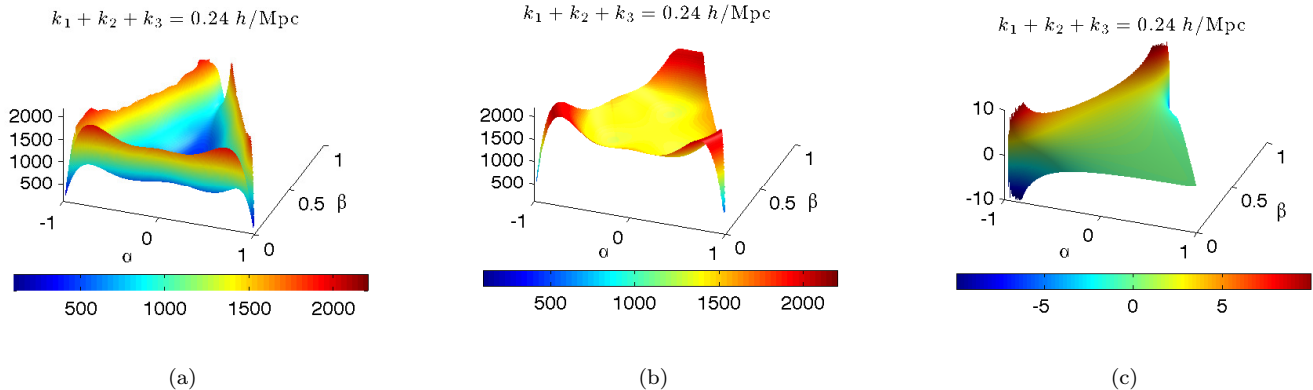


Figure 2. Two-dimensional slices of (a) the leading order gravitational bispectrum B_{δ}^{grav} from (7), (b) the expression $2P_{\delta}^L(k_1)P_{\delta}^L(k_2) + \text{perms}$ and (c) the kernel $F_2^{(s)}$ defined in (6) (with cut-offs in the squeezed limit where the kernel diverges). All slices are at fixed $k_1 + k_2 + k_3 = 0.24h/\text{Mpc}$ and we restrict the plot to $k_i \geq 0.0013h/\text{Mpc}$, corresponding to a $5000\text{Mpc}/h$ box. The linear power spectra are evaluated at $z = 30$.

expression (7) for Gaussian initial conditions, that is,

$$B_{\delta, \text{NL}}^{\text{grav}} \equiv 2P_{\delta}(k_1)P_{\delta}(k_2)F_2^{(s)}(\mathbf{k}_1, \mathbf{k}_2) + 2 \text{ perms.} \quad (8)$$

We will find the expression (8) to be a key approximation to the full gravitational bispectrum as we probe beyond the mildly nonlinear regime later. Of course, this omits several loop corrections containing powers of $F_2^{(s)}$ or higher order kernels, but it is easy to evaluate with the nonlinear power spectrum from CAMB [28]. We will discuss further loop corrections much more quantitatively in a forthcoming publication [35].

Halo models

At sufficiently small scales, well probed by our simulations, the perturbative treatment breaks down and simulations and phenomenological models must be used. In the strongly nonlinear regime the halo model can be used as a phenomenological model for the dark matter distribution (see [36] for a review). Recently in Ref. [37] it was demonstrated that combining 1-loop perturbation theory with the halo model describes the matter bispectrum in simulations at the $\mathcal{O}(10\%)$ level on nonlinear scales for equilateral and isosceles bispectrum slices. Similar results were obtained in Ref. [38], where local non-Gaussian initial conditions were also considered and compared with simulations for $k \leq 0.3h/\text{Mpc}$ at $z \leq 1$. In the mildly nonlinear regime, when the approximation that all dark matter particles are inside halos is no longer valid, the halo model becomes less accurate than in the strongly nonlinear regime. It should also be noted that important ingredients of the halo model like the halo density profile and halo mass function cannot be derived analytically but are obtained from fits to N -body simulations.

In detail, the halo model prediction for the dark matter bispectrum is given by three contributions corresponding to the three cases that the three points of the three point function lie in one, two or three halos (see e.g. [36–38]):

$$B_{\text{HM}} = B_{1\text{H}} + B_{2\text{H}} + B_{3\text{H}}, \quad (9)$$

where

$$B_{1\text{H}}(k_1, k_2, k_3) = \frac{1}{\bar{\rho}^3} \int dm n(m) \prod_{i=1}^3 \hat{\rho}(k_i, m), \quad (10)$$

$$B_{2\text{H}}(k_1, k_2, k_3) = \frac{1}{\bar{\rho}^3} \int dm_1 n(m_1) \hat{\rho}(k_1, m_1) \int dm_2 n(m_2) \hat{\rho}(k_2, m_2) \hat{\rho}(k_3, m_2) P_h(k_1, m_1, m_2) + \text{perms}, \quad (11)$$

$$B_{3\text{H}}(k_1, k_2, k_3) = \frac{1}{\bar{\rho}^3} \left[\prod_{i=1}^3 \int dm_i n(m_i) \hat{\rho}(k_i, m_i) \right] B_h(k_1, m_1; k_2, m_2; k_3, m_3). \quad (12)$$

Here $n(m)$ is the mass function and $\hat{\rho}(k, m)$ is the Fourier transform of the density profile of a halo of mass m , i.e. for spherically symmetric density profiles (like the commonly used NFW profile [39])

$$\hat{\rho}(k, m) = 4\pi \int dr r^2 \rho(r, m) \frac{\sin(kr)}{kr}. \quad (13)$$

P_h and B_h denote the halo power spectrum and bispectrum, which can be related to the tree level dark matter power spectrum and bispectrum on large scales using bias relations.

Constant ‘halo’ model

As we consider the more strongly nonlinear regime, $k \geq 1h/\text{Mpc}$ at $z = 0$, the halo model bispectrum is dominated by the 1-halo contribution $B_{1\text{H}}$. Neglecting the overall bispectrum amplitude, we find that in this regime the 1-halo shape for Gaussian initial conditions can be approximated by a simple constant bispectrum,

$$B_{\delta,\text{const}}^{\text{grav}}(k_1, k_2, k_3)|_z \equiv c_1 \bar{D}^{n_h}(z) (k_1 + k_2 + k_3)^\nu. \quad (14)$$

Here, ‘constant’ refers to constancy on $k_1 + k_2 + k_3 = \text{const.}$ slices (see [7]), noting that this is a bispectrum typical of isolated point-like objects (e.g. particles randomly distributed in a box have a completely constant shot noise bispectrum). The expression (14) has an overall wavenumber scale-dependence with exponent ν and a time-dependence on the linear growth function $\bar{D}(z)$ with halo exponent n_h . The wavenumber scaling $\nu \approx -1.7$ is chosen such that it approximately reflects the scaling for equilateral triangle configurations in this regime as measured in our simulations (and which is approximately predicted by the halo model for Gaussian initial conditions [37, 38]). The exponent n_h is similarly defined by the fast growth factor appropriate for the halo model for the scales under study $0.2h/\text{Mpc} \lesssim k \leq 2h/\text{Mpc}$, typically with $n_h \approx 6-8$. For $k_{\text{max}} = 2h/\text{Mpc}$ and $z = 0$, this simple model achieves a shape correlation of 99.7% with the 1-halo contribution $B_{1\text{H}}$ and 99.3% with the full halo model bispectrum (9).

In later sections, we will note that (14) provides an excellent approximation to the late-time bispectrum in the nonlinear regime when we use it in a simple fitting formula together with the modified tree-level gravitational bispectrum (8). We shall investigate the other halo contributions in more detail elsewhere [35].

As we shall see, on smaller nonlinear scales (large $k > 1h/\text{Mpc}$) the fast bispectrum growth begins to slow down by the present day $z = 0$. In this case, we should really replace the power law growth $D^{n_h}(z)$ for the constant mode using a more general growth factor $\mathcal{T}(\tilde{k}, z, z_i)$, where the ‘slice’ or ‘average’ wavenumber

$$\tilde{k} = (k_1 + k_2 + k_3)/3. \quad (15)$$

For future reference, it is convenient to use this growth rate in a more general integral form of the ‘constant’ model (14), that is,

$$\begin{aligned} B_{\delta,\text{const}}^{\text{grav}}(k_1, k_2, k_3)|_z &\equiv \mathcal{T}(\tilde{k}, z, z_i) B_{\text{const}}^{\text{init}}(\tilde{k}, z_i) \quad (16) \\ &\equiv \int_{z_i}^z \mathcal{G}(\tilde{k}, z) dz B_{\text{const}}^{\text{init}}(\tilde{k}, z_i), \end{aligned}$$

where z_i is the redshift at which this rapid ‘halo’ growth takes hold (it has an implicit \tilde{k} dependence). The quantity $B_{\text{const}}^{\text{init}}(\tilde{k}, z_i)$ represents the initial condition at $z = z_i$ for the constant part of the bispectrum. Naively, we

might take this to be $B_{\text{const}}^{\text{init}}(\tilde{k}, z_i) = B_{\delta}^{\text{grav}}(\tilde{k}, \tilde{k}, \tilde{k})|_{z=z_i}$, that is, the equilateral or constant part of the tree-level gravitational bispectrum (7) at $z = z_i$. However, to date, determining the amplitude of this initial constant bispectrum has relied on simulations. We will use this simple model to characterise both the time- and scale-dependence of the gravitational bispectrum, as well as primordial non-Gaussianity as we approach the strongly nonlinear regime.

Alternative phenomenological fit

An alternative description of the gravitational matter bispectrum in the non-perturbative regime was proposed in Ref. [13], who constructed a fitting formula which interpolates between the perturbative prediction on large scales and a local-type bispectrum on small scales, which was suggested by early simulations. In their terminology, the small-scale bispectrum was denoted as a ‘constant reduced’ bispectrum, which implies that it takes the same form as the local shape $B_{\delta} \sim P_{\delta}(k_1)P_{\delta}(k_2) + \text{perms}$, in contrast to the constant shape (14) above. Recently Ref. [14] extended this fitting formula with updated simulations into mildly nonlinear scales $0.03h/\text{Mpc} \leq k \leq 0.4h/\text{Mpc}$ at $0 \leq z \leq 1.5$.

We review for the sake of completeness this phenomenological 9-parameter fit, for which we will test the regime of validity. The linear power spectrum in (7) is replaced by the nonlinear one P_{δ} , and the symmetrised kernel $F_2^{(s)}$ is replaced by

$$\begin{aligned} F_2^{(s)\text{eff}}(\mathbf{k}_1, \mathbf{k}_2) &= \frac{5}{7} a(n_1, k_1) a(n_2, k_2) \\ &+ \frac{1}{2} \frac{\mathbf{k}_1 \cdot \mathbf{k}_2}{k_1 k_2} \left(\frac{k_1}{k_2} + \frac{k_2}{k_1} \right) b(n_1, k_1) b(n_2, k_2) \\ &+ \frac{2}{7} \left(\frac{\mathbf{k}_1 \cdot \mathbf{k}_2}{k_1 k_2} \right)^2 c(n_1, k_1) c(n_2, k_2), \quad (17) \end{aligned}$$

where

$$a(n, k) = \frac{1 + \sigma_8^{a_6}(z) \sqrt{0.7 Q_3(n)} (a_1 q)^{a_2 + n}}{1 + (a_1 q)^{a_2 + n}}, \quad (18)$$

$$b(n, k) = \frac{1 + 0.2 a_3 (n + 3) (q a_7)^{n+3+a_8}}{1 + (q a_7)^{3.5+n+a_8}}, \quad (19)$$

$$c(n, k) = \frac{1 + 4.5 a_4 / [1.5 + (n + 3)^4] (q a_5)^{n+3+a_9}}{1 + (q a_5)^{3.5+n+a_9}}. \quad (20)$$

In these formulae, n represents the slope of the linear power spectrum at k , i.e. $n = d \ln P_{\delta}^L(k) / d \ln k$ (with an additional spline interpolation as described in [14]), $q = k/k_{\text{nl}}$ with k_{nl} defined by $k_{\text{nl}}^3 P_{\delta}^L(k_{\text{nl}}) / (2\pi^2) = 1$, and the function $Q_3(n)$ is given by

$$Q_3(n) = \frac{4 - 2^n}{1 + 2^{n+1}}. \quad (21)$$

The best-fit values for the free parameters $a_1 - a_9$ were found by simulations [14]

$$\begin{aligned} a_1 &= 0.484, & a_2 &= 3.740, & a_3 &= -0.849, \\ a_4 &= 0.392, & a_5 &= 1.013, & a_6 &= -0.575, \\ a_7 &= 0.128, & a_8 &= -0.722, & a_9 &= -0.926. \end{aligned} \quad (22)$$

III. PRIMORDIAL NON-GAUSSIANITY

Additional to the contribution B_δ^{grav} from nonlinear gravity, the matter bispectrum can have primordial contributions B_δ^{prim} from inflation or some other early universe model such as cosmic defects. While the simple model of single field slow roll inflation gives only a small primordial bispectrum, $f_{\text{NL}} \sim \mathcal{O}(10^{-2})$, other models can yield large non-Gaussianities with $f_{\text{NL}} > 1$ (see e.g. [40–44] for reviews). Such models can be distinguished if they induce different bispectrum shapes, i.e. different dependencies of the bispectra on the momenta k_1, k_2, k_3 as illustrated in Fig. 3. However, before reviewing primordial bispectrum shapes we describe how primordial non-Gaussianity changes the dark matter bispectrum.

Primordial contribution to the matter bispectrum

Let us assume that an inflationary model produces a primordial bispectrum B_Φ with nonlinear amplitude f_{NL} , i.e.²

$$\langle \Phi(\mathbf{k}_1)\Phi(\mathbf{k}_2)\Phi(\mathbf{k}_3) \rangle = (2\pi)^3 \delta_D(\Sigma_i \mathbf{k}_i) f_{\text{NL}} B_\Phi(k_1, k_2, k_3). \quad (23)$$

From the linear Poisson equation (2) we see that the primordial contribution to the matter bispectrum is given at leading order by

$$B_\delta^{\text{prim}}(k_1, k_2, k_3)|_z = M(k_1, z)M(k_2, z)M(k_3, z)f_{\text{NL}}B_\Phi(k_1, k_2, k_3), \quad (24)$$

which is valid on large scales.

A simple improvement to the tree level shape which incorporates some loop corrections can be obtained with the nonlinear power spectrum P_δ :

$$B_{\delta, \text{NL}}^{\text{prim}}(k_1, k_2, k_3) \equiv \sqrt{\frac{P_\delta(k_1)P_\delta(k_2)P_\delta(k_3)}{P_\Phi(k_1)P_\Phi(k_2)P_\Phi(k_3)}} B_\Phi(k_1, k_2, k_3), \quad (25)$$

where $P_\Phi(k_i)$ refers to the primordial power spectrum at some early time in matter domination. As will be demonstrated later in this paper, this shape can be used to obtain simple fitting formulae for the primordial contribution to the matter bispectrum. A more systematic but also more cumbersome approach is to include loop corrections, which become important on small scales [11, 12]. We shall calculate more of these contributions in a subsequent paper and test their correspondence to the N -body simulations [35].

We note that, while the time dependence of the tree level gravitational bispectrum (7) is given by $B_\delta^{\text{grav}} \propto D^4(z)$, the tree level primordial contribution (24) only grows like $B_\delta^{\text{prim}} \propto D^3(z)$, implying that it is easier to extract the primordial contribution to the dark matter bispectrum at early times. The simulations and fitting formulae discussed later will show that the gravitational bispectrum also grows faster than the primordial contribution in the strongly nonlinear regime (also by a factor of roughly $D(z)$).

Non-Gaussianity as a halo model time-shift

At sufficiently small scales the perturbative treatment breaks down and simulations and phenomenological models must be used. The phenomenological halo model prediction for local non-Gaussian initial conditions was computed in [38] by incorporating modified expressions for the halo model ingredients in presence of local non-Gaussianity. While first tests by [38] demonstrate that this approach works well for some one-dimensional bispectrum slices in the mildly nonlinear regime, $k \leq 0.3h/\text{Mpc}$ and $z \leq 1$, comparisons to simulations in the strongly nonlinear regime have not been undertaken to date.

An alternative phenomenological model we propose here is to note that the primordial bispectrum can also contribute to the halo model bispectrum as an initial offset or time-shift. As we have seen the 1-halo model is highly correlated with the simple ‘constant’ bispectrum we described earlier (14). The key point is that this constant halo contribution grows much more rapidly than both the tree-level primordial bispectrum (24) or the tree-level gravitational bispectrum (7). Consequently, if the primordial bispectrum has a significant positive (or negative) constant component, then this can act as an initial condition for the halo bispectrum; the faster halo amplification growth will start earlier (or later) by a time or redshift offset Δz . The constant part of the primordial signal, then, will participate in the halo bispectrum growth and can be amplified much faster than expected from the tree-level result (24) or even with loop corrections (25). If this physical picture is correct, then the primordial constant contribution can be described perturbatively around the constant halo bispectrum (14) by

² Non-linear corrections to the mapping between \mathcal{R} and Φ , which are not taken into account here, induce an additional bispectrum of Φ , which is however smaller than the primordial contributions considered here [42].

$$z = 30$$

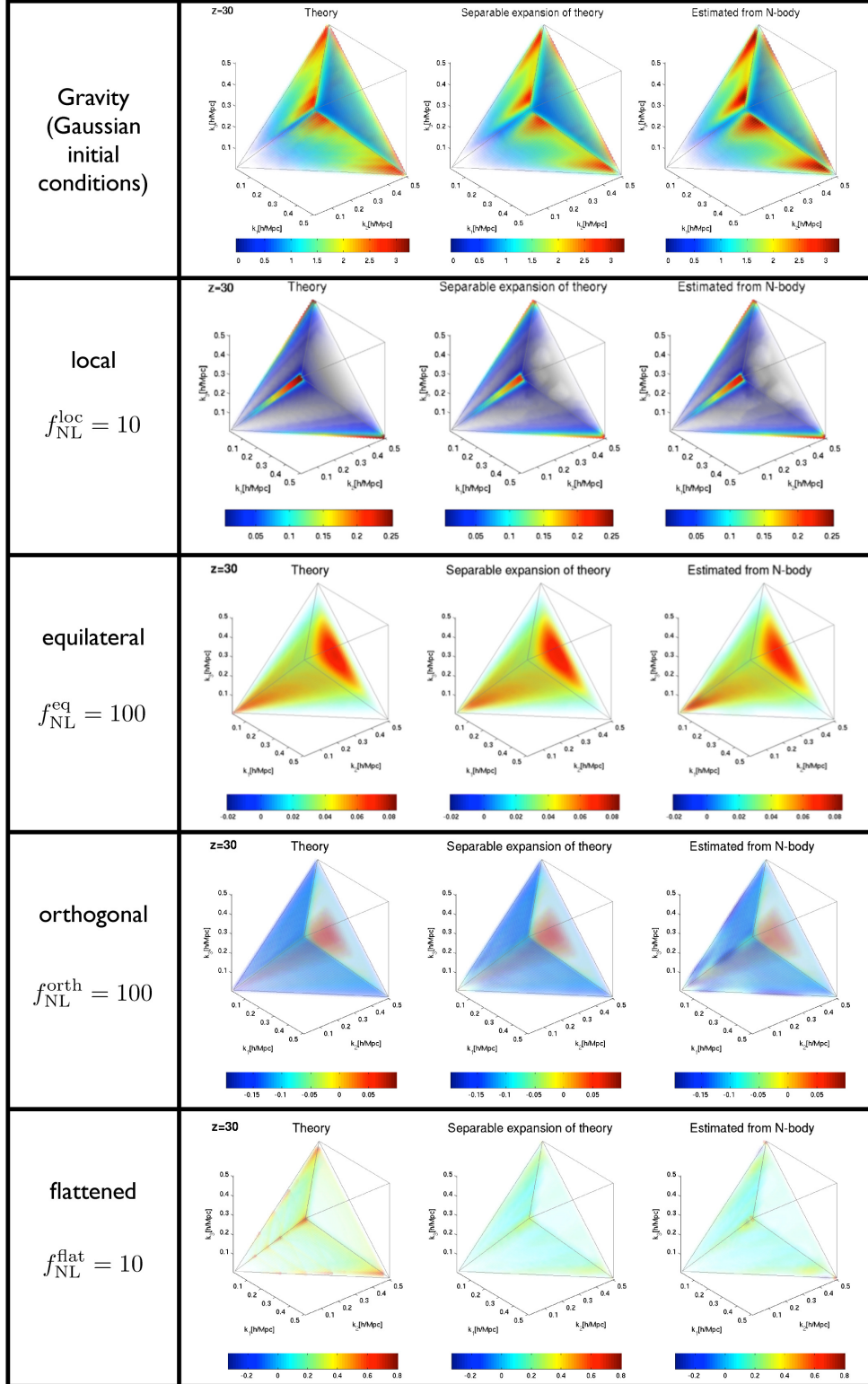


Figure 3. Illustration of separable expansion (44) for some theoretical tree level bispectra. Each black cell of 3 plots contains from left to right: Theoretical tree level prediction (7) or (24), separable expansion of the tree level theory (44) and estimated bispectrum from N -body simulations (56) (for simulations G512b, Loc10, Eq100, Orth100 and Flat10 from top to bottom). The plots show signal to noise weighted bispectra (as on the left hand side of (44)) on the tetrapyd domain in Fig. 1, evaluated at redshift $z = 30$ for 512^3 particles in a box with $L = 1600\text{Mpc}/h$. The opaqueness of the points reflects the absolute value of the signal to noise weighted bispectrum (values close to 0 are completely transparent). Colors and transparency are consistent within each black cell but differ across different black cells. The plot axes are $k_1, k_2, k_3 \leq 0.5h/\text{Mpc}$. For better visibility we do not plot points with $k_1 + k_2 + k_3 > 2k_{\text{max}}$ (corresponding to the green region in Fig. 1).

expanding the growth factor

$$\bar{D}^{n_h}(z + \Delta z) \approx \bar{D}^{n_h}(z) + n_h \bar{D}^{n_h-1}(z) \frac{d\bar{D}(z)}{dz} \Delta z. \quad (26)$$

We determine Δz by matching the projection of the total measured bispectrum \hat{B}_δ on the constant shape $B_{\delta, \text{const}}^{\text{grav}}$ in the Gaussian and non-Gaussian simulations:

$$(\hat{f}_{\text{NL}}^{\text{const}})_{\text{Gauss}}(z + \Delta z) = (\hat{f}_{\text{NL}}^{\text{const}})_{\text{NG}}(z). \quad (27)$$

From simulations, the time shift Δz and the corresponding shift of the growth function, $\Delta \bar{D} = \frac{d\bar{D}(z)}{dz} \Delta z$, are both found to vary over time at most by a factor of 2 for redshifts $10 \gtrsim z \gtrsim 1$ for local, equilateral and flattened initial conditions (to the extent to which this can be tested by linearly interpolating the limited number of output redshifts at which the bispectrum was measured). Provided $\Delta \bar{D}$ is time-independent this perturbation of the simple ‘constant’ model (14) means we should be able to model the halo contribution from the primordial perturbation as

$$B_{\delta, \text{const}}^{\text{prim}}(k_1, k_2, k_3) \equiv c_2 \bar{D}^{n_h^{\text{prim}}}(z) (k_1 + k_2 + k_3)^\nu, \quad (28)$$

where we expect $n_h^{\text{prim}} = n_h - 1$ from (26) and again $\nu \approx -1.7$. The fitting parameter c_2 will be related to the correlation between the primordial shape³ and the constant model at the time at which halos form for the length scale under consideration. Different non-Gaussian bispectrum models should show consistent behaviour in the nonlinear regime depending on the relative magnitude of their constant component. We shall define these quantities more precisely after introducing the bispectrum shape correlator in the next section, but (28) will be an important component in our later fitting formulae for primordial non-Gaussianity.

The simple power law in the linear growth function $\bar{D}(z)$ used to model the time dependence of the constant halo bispectrum can of course be extended to more general functions of time (16), whose time derivative would then enter in the expansion (26). The results presented later show that the overall normalisation of the simple fits can be improved by a more general modeling of the time dependence (reducing the overall growth rate in the strongly nonlinear regime). In this case, we can consider

³ We refer here to the excess bispectrum compared to Gaussian initial conditions as measured in N -body simulations at times when the constant contribution to the bispectrum is not negligible compared to the partially loop-corrected tree level contribution (25). Therefore c_2 is a fitting parameter to be determined from N -body simulations.

a time-shift for the more general ‘constant’ model (16)

$$\begin{aligned} B_{\delta, \text{const}}^{\text{prim}}(k_1, k_2, k_3)|_z &= B_{\delta, \text{const}}^{\text{grav}}(k_1, k_2, k_3)|_{z+\Delta z} \\ &\quad - B_{\delta, \text{const}}^{\text{grav}}(k_1, k_2, k_3)|_z \\ &= \frac{d\mathcal{T}(\tilde{k}, z, z_i)}{dz} B_{\text{const}}^{\text{init}}(\tilde{k}, z_i) \Delta z + \dots, \end{aligned} \quad (29)$$

where we neglect higher order terms assuming them to be subdominant. We can determine the time-shift Δz by determining the magnitude of the constant part of the primordial bispectrum at $z = z_i$.

While more sophisticated models of the time evolution are left for future work, we note that the correlation with the measured bispectrum shape cannot be improved much, because simulations are so well described by a combination of the ‘constant’ shape (28) and the modified tree-level gravitational shape (25) used in the fitting formulae presented later.

Primordial bispectrum shapes from inflation

Local shape

The fiducial f_{NL} model of primordial non-Gaussianity is the local model [45], which is described in this way because it can be generated simply by squaring a Gaussian field Φ_G in real space,

$$\Phi(\mathbf{x}) = \Phi_G(\mathbf{x}) + f_{\text{NL}}[\Phi_G^2(\mathbf{x}) - \langle \Phi_G^2 \rangle], \quad (30)$$

where $\langle \Phi_G^2 \rangle$ denotes an average over \mathbf{x} space and ensures that the average perturbation is zero. The resulting bispectrum takes the form

$$B_\Phi^{\text{loc}}(k_1, k_2, k_3) = 2 [P_\Phi(k_1)P_\Phi(k_2) + 2 \text{ perms}], \quad (31)$$

which is illustrated in Fig. 3 and peaks at squeezed triangle configurations, where one wavenumber is much smaller than the other two. Multiple field inflation models are one potential source of this shape (for a review see [40]). If a bispectrum signal in the squeezed limit is detected, then this will rule out all canonical single field models of inflation [46–48].

Equilateral shape

Higher derivative operators in the inflationary action, arising e.g. in DBI inflation [49] and in effective field theory approaches [48, 50], produce a shape that can be approximated by the separable equilateral template [24, 40, 51]

$$\begin{aligned} B_\Phi^{\text{eq}} &= 6 [- (P_\Phi(k_1)P_\Phi(k_2) + 2 \text{ perms}) \\ &\quad - 2(P_\Phi(k_1)P_\Phi(k_2)P_\Phi(k_3))^{2/3} \\ &\quad + (P_\Phi^{1/3}(k_1)P_\Phi^{2/3}(k_2)P_\Phi(k_3) + 5 \text{ perms})], \end{aligned} \quad (32)$$

which peaks in the equilateral limit, $k_1 = k_2 = k_3$. For equilateral triangles with $k_1 = k_2 = k_3$ summing up the corresponding three plane waves, $\sum_j \Phi(\mathbf{k}_j) e^{i\mathbf{k}_j \mathbf{x}}$, gives filamentary overdensities, i.e. overdense cylinders along the direction perpendicular to the plane of the triangle of $(\mathbf{k}_1, \mathbf{k}_2, \mathbf{k}_3)$, surrounded by underdensities (as motivated in Ref. [52]). A primordial equilateral shape from higher derivatives, therefore, must be distinguished carefully from the stronger equilateral and (highly correlated) constant contribution produced at late times by nonlinear gravitational collapse and the emergence of filamentary and point-like structures (see e.g. [31, 33]). We will confirm this expectation by measuring the bispectrum in N -body simulations.

Orthogonal shape

Another shape that can arise from single field inflation is the orthogonal shape [53], which is roughly orthogonal to the equilateral and the local shape and peaks (with opposite sign) for both equilateral and flattened/elongated triangle configurations ($k_3 = k_1 + k_2$). It can be approximated by the separable template [53]

$$B_{\Phi}^{\text{orth}} = 6[3(P_{\Phi}^{1/3}(k_1)P_{\Phi}^{2/3}(k_2)P_{\Phi}(k_3) + 5 \text{ perms}) - \frac{3}{2}B_{\Phi}^{\text{loc}} - 8(P_{\Phi}(k_1)P_{\Phi}(k_2)P_{\Phi}(k_3))^{2/3}]. \quad (33)$$

Being orthogonal to the equilateral shape, the constant mode is relatively suppressed, a fact which will be important in later discussions. We note that all the shapes above (31)–(33) are written explicitly as the sum of separable functions of the wavenumbers k_1, k_2, k_3 .

Flattened shape

A non-Bunch-Davies vacuum leads to shapes which peak for flattened/elongated ($k_1 + k_2 = k_3$) and folded ($k_1 = 2k_2 = 2k_3$) triangle configurations⁴ [40, 54–56]. This flattened shape depends on terms such as $1/(k_1 + k_2 - k_3)$ [54]. Therefore it provides an important example of a bispectrum which is inherently non-separable, so it is computationally difficult to generate initial conditions for this shape and to extract its amplitude from data. We will use an expansion in separable modes to solve both problems [7, 8, 26, 27]. Of course, there is a divergence for elongated triangles, $k_3 = k_1 + k_2$, which must be removed with a physically motivated cutoff. For definiteness we use the same shape and cutoff

⁴ Sometimes other names are used for these triangles, we follow [34].

as was used for the CMB in [2, 7], setting $B = 0$ for $k_1 + k_2 - k_3 < 0.03(k_1 + k_2 + k_3)$ and permutations, and then smoothing on $k_1 + k_2 + k_3 = \text{const.}$ slices with a Gaussian filter with FWHM of $0.03/(k_1 + k_2 + k_3)$.

It is worth noting that the equilateral and orthogonal templates are separable approximations of inflationary shapes, with good agreement where the primordial bispectrum signal peaks. However late time observables may be sensitive to suppressed triangle configurations for which template and physical shape may differ significantly (e.g. scale dependent halo bias mainly depends on the squeezed limit of the bispectrum [24, 57]). The methods described below enable us to simulate and estimate physical non-separable bispectra without using such separable templates. However we do not expect significant differences for the dark matter bispectrum, because its peaks are well approximated by the separable templates. For this reason and for easier comparability with other simulations, we use the equilateral and orthogonal templates instead of the physical shapes. Future work, especially on the power spectrum and bispectrum of halos, will instead focus on the physical shapes.

IV. BISPECTRUM ESTIMATION METHODOLOGY

f_{NL} estimator

If our theoretical model is that the density perturbation δ has power spectrum $P_{\delta}(k)$ and bispectrum $f_{\text{NL}}^{\text{th}} B_{\delta}^{\text{th}}$, then the maximum likelihood estimator for the amplitude of this bispectrum in the limit of weak non-Gaussianity is given by [26, 27]⁵

$$\hat{f}_{\text{NL}}^{\text{th}} = \frac{(2\pi)^3}{N_{\text{th}}} \int \frac{\prod_{i=1}^3 d^3 \mathbf{k}_i}{(2\pi)^9} (2\pi)^3 \delta_D(\mathbf{k}_1 + \mathbf{k}_2 + \mathbf{k}_3) \times \frac{B_{\delta}^{\text{th}}(k_1, k_2, k_3) [\delta_{\mathbf{k}_1} \delta_{\mathbf{k}_2} \delta_{\mathbf{k}_3} - 3 \langle \delta_{\mathbf{k}_1} \delta_{\mathbf{k}_2} \rangle \delta_{\mathbf{k}_3}]}{P_{\delta}(k_1) P_{\delta}(k_2) P_{\delta}(k_3)} \quad (34)$$

where δ is the observed density perturbation. If this has a bispectrum B_{δ}^{obs} , i.e.

$$\langle \delta_{\mathbf{k}_1} \delta_{\mathbf{k}_2} \delta_{\mathbf{k}_3} \rangle = (2\pi)^3 \delta_D(\Sigma_i \mathbf{k}_i) B_{\delta}^{\text{obs}}(k_1, k_2, k_3), \quad (35)$$

⁵ In the denominator we have assumed that $\langle \delta \delta \rangle$ is diagonal which is valid for a statistically homogeneous density perturbation. The linear term $\langle \delta \delta \rangle \delta$ in the numerator is written out for completeness but it is not used in our simulations because it vanishes for a statistically homogeneous field (because $\delta_{\mathbf{k}=0} = 0$).

then the expectation value of (34) is given by⁶

$$\langle \hat{f}_{\text{NL}}^{\text{th}} \rangle = \frac{1}{N_{\text{th}}} \frac{V}{\pi} \int_{\mathcal{V}_B} dV_k k_1 k_2 k_3 \times \frac{B_\delta^{\text{obs}}(k_1, k_2, k_3) B_\delta^{\text{th}}(k_1, k_2, k_3)}{P_\delta(k_1) P_\delta(k_2) P_\delta(k_3)}, \quad (36)$$

where $dV_k \equiv dk_1 dk_2 dk_3$, \mathcal{V}_B is the tetrahedral domain allowed by the triangle condition on the wavenumbers k_i , and V is a volume factor given by $V = (2\pi)^3 \delta_D(\mathbf{0}) = L^3$. Demanding $\langle \hat{f}_{\text{NL}}^{\text{th}} \rangle = 1$ for $B_\delta^{\text{th}} = B_\delta^{\text{obs}}$ fixes the normalisation such that

$$N_{\text{th}} = \frac{V}{\pi} \int_{\mathcal{V}_B} dV_k \frac{k_1 k_2 k_3 [B_\delta^{\text{th}}(k_1, k_2, k_3)]^2}{P_\delta(k_1) P_\delta(k_2) P_\delta(k_3)}. \quad (37)$$

Shape and size comparisons

Eq. (36) motivates the definition of a scalar product between two bispectrum shapes [26, 58],

$$\langle B_i, B_j \rangle \equiv \frac{V}{\pi} \int_{\mathcal{V}_B} dV_k \frac{k_1 k_2 k_3 B_i(k_1, k_2, k_3) B_j(k_1, k_2, k_3)}{P_\delta(k_1) P_\delta(k_2) P_\delta(k_3)}, \quad (38)$$

which can be normalised to a number between -1 and 1 by defining the cosine or shape correlation

$$\mathcal{C}(B_i, B_j) \equiv \frac{\langle B_i, B_j \rangle}{\sqrt{\langle B_i, B_i \rangle \langle B_j, B_j \rangle}}. \quad (39)$$

If two theoretical bispectra B_1 and B_2 have a small shape correlation, $|\mathcal{C}(B_1, B_2)| \ll 1$, the optimal estimator for $f_{\text{NL}}^{B_1}$ will perform badly in detecting $f_{\text{NL}}^{B_2}$ and vice versa. Therefore the shape correlation is a useful measure of the similarity of bispectrum shapes.

To measure the total integrated size of a bispectrum we define the squared norm as the cumulative signal to noise squared of the bispectrum [2, 51],

$$\|B\|^2 \equiv \frac{V}{(2\pi)^3} \int_{\mathcal{V}_B} dV_k \frac{s_B}{6} \frac{B^2(k_1, k_2, k_3)}{\text{var } B(k_1, k_2, k_3)} = \frac{\langle B, B \rangle}{6(2\pi)^3}, \quad (40)$$

which equals the quantity $(S/N)_B^2$ in [17]. The symmetry factor s_B is 6 if $k_1 = k_2 = k_3$, 2 if only two k_i equal each other and 1 if all k_i are different from each other. To obtain the expression on the right hand side of (40) we assumed that different Fourier modes are uncorrelated,

⁶ Performing the angular integrals shows for arbitrary $F(k_1, k_2, k_3)$

$$\int \frac{\prod_{i=1}^3 d^3 \mathbf{k}_i}{(2\pi)^9} (2\pi)^6 \delta_D^2(\sum_{j=1}^3 \mathbf{k}_j) F = \frac{V}{8\pi^4} \int_{\mathcal{V}_B} dk_1 dk_2 dk_3 k_1 k_2 k_3 F,$$

which corrects for a factor of $(2\pi)^3$ missing in [26, 27].

$\langle \delta_{\mathbf{k}} \delta_{\mathbf{k}'} \rangle \propto \delta_D(\mathbf{k} + \mathbf{k}')$, and we only took the Gaussian contribution to the bispectrum noise into account, i.e.⁷

$$\text{var } B(k_1, k_2, k_3) = (2\pi)^3 \frac{s_B P_\delta(k_1) P_\delta(k_2) P_\delta(k_3)}{8\pi^2 k_1 k_2 k_3}. \quad (41)$$

It is also convenient to normalise the total integrated bispectrum size with respect to the linearly evolved local bispectrum defined in (31) and (24) (see [2] for a similar quantity in the CMB context):

$$\bar{F}_{\text{NL}}^B \equiv \frac{\|B\|}{\|B_\delta^{\text{prim,loc}}\|}. \quad (42)$$

We use the *linearly* evolved local bispectrum without loop corrections to obtain an expression which can be easily evaluated.

Using definitions (39) and (40), the expectation value (36) can be rewritten in the intuitive form

$$\langle \hat{f}_{\text{NL}}^{\text{th}} \rangle = \mathcal{C}(B_\delta^{\text{th}}, B_\delta^{\text{obs}}) \frac{\|B_\delta^{\text{obs}}\|}{\|B_\delta^{\text{th}}\|}. \quad (43)$$

Therefore the bispectrum amplitude f_{NL} can be interpreted as the projection of the observed bispectrum shape on the theoretical bispectrum shape, which is given by the cosine of the shapes times the ratio of their norms.

Separable mode expansion for fast f_{NL} estimation

Evaluating the estimator (34) is computationally very expensive because it requires $\mathcal{O}(N^6)$ operations for a grid with N points per dimension (typically $N = \mathcal{O}(10^3)$). For an efficient evaluation we expand the signal to noise weighted theoretical bispectrum in the separable form

$$\frac{\sqrt{k_1 k_2 k_3} B_\delta^{\text{th}}(k_1, k_2, k_3)}{\sqrt{P_\delta(k_1) P_\delta(k_2) P_\delta(k_3)}} = \sum_{n=0}^{n_{\text{max}}-1} \alpha_n^Q q_{\{r\}}(k_1) q_s(k_2) q_t(k_3), \quad (44)$$

where $\{rst\}$ denotes a symmetrisation over the indices, and a partial ordering has been introduced to enumerate the modes (for a fuller description see [8]). The expressions q_r could be any set of independent one-dimensional basis functions. For definiteness we choose q_r to be polynomials of order r defined in [8] and choose the slice ordering defined in Eq. (58) of [8]. We truncate the modal expansion (44) after $n_{\text{max}} = \mathcal{O}(50)$ modes, which provides an accurate representation for the shapes we are considering as illustrated in Fig. 3, which compares theoretical bispectra on the left with truncated expansions

⁷ We need an additional factor of $(2\pi)^3$ compared to [17] because $P_{\text{them}} = (2\pi)^3 P_{\text{us}}$ and $B_{\text{them}} = (2\pi)^3 B_{\text{us}}$.

in the centre (and bispectra measured in N-body simulations on the right). More quantitative discussions of the error induced by the truncation of the expansions will be provided later in terms of shape correlations.

The separable expansion (44) allows us to write the estimator and its expectation value in the form

$$\hat{f}_{\text{NL}}^{\text{th}} = \frac{(2\pi)^3}{N_{\text{th}}} \sum_n \alpha_n^Q \int d^3\mathbf{x} [M_r(\mathbf{x})M_s(\mathbf{x})M_t(\mathbf{x}) - 3\langle M_{\{r}(\mathbf{x})M_s(\mathbf{x})\}M_t(\mathbf{x})\rangle], \quad (45)$$

$$\langle \hat{f}_{\text{NL}}^{\text{th}} \rangle = \frac{1}{N_{\text{th}}} \sum_{nm} \alpha_n^Q \alpha_m^Q \gamma_{nm}, \quad (46)$$

where

$$\begin{aligned} \gamma_{nm} &= \frac{V}{\pi} \int_{\mathcal{V}_B} dV_k Q_n(k_1, k_2, k_3) Q_m(k_1, k_2, k_3), \\ M_r(\mathbf{x}) &= \int \frac{d^3\mathbf{k}}{(2\pi)^3} \frac{\delta_{\mathbf{k}} q_r(k)}{\sqrt{k} P_\delta(k)} e^{i\mathbf{k}\cdot\mathbf{x}} \end{aligned} \quad (47)$$

and

$$Q_n(k, k', k'') \equiv q_{\{r}(k)q_s(k')q_t(k''). \quad (48)$$

This form of the estimator can be evaluated efficiently because it involves only Fourier transforms and one three-dimensional integral over position space, leading to $\mathcal{O}(N^3)$ operations.

To motivate the choice of the prefactor in the expansion (44) let us transform to basis functions $R_n(k_1, k_2, k_3)$ that are orthonormal on the tetrapyd domain, $\langle R_n, R_m \rangle_{\text{noweight}} = \delta_{nm}$, with respect to the unweighted scalar product

$$\langle B_i, B_j \rangle_{\text{noweight}} \equiv \frac{V}{\pi} \int_{\mathcal{V}_B} dV_k B_i(k_1, k_2, k_3) B_j(k_1, k_2, k_3). \quad (49)$$

From $\sum_n \alpha_n^Q Q_n = \sum_n \alpha_n^R R_n$ and Eq. (44) we find that

$$B_\delta^{\text{th}}(k_1, k_2, k_3) = \sum_n \alpha_n^R B_n^R(k_1, k_2, k_3), \quad (50)$$

where the contributions

$$B_n^R(k_1, k_2, k_3) \equiv \sqrt{\frac{P_\delta(k_1)P_\delta(k_2)P_\delta(k_3)}{k_1 k_2 k_3}} R_n(k_1, k_2, k_3) \quad (51)$$

to the full bispectrum are orthonormal with respect to (38). Thus the expansion coefficients α_n^R measure the size of contributions to the bispectrum which are orthonormal with respect to the signal to noise weighted scalar product (38).

As a side remark, note that in contrast to the signal to noise weighted scalar product (38) induced by the estimator expectation value, the weight of the scalar product (49) is time-independent and does not depend on the

range of scales under consideration. Therefore we can use the same set of orthonormal polynomials R_n at any time and for all length scales. If the expansion (44) does not converge as well as for the applications considered here, different (separable) scalar product weights can be used to orthonormalise the R_n 's.

Fast modal bispectrum estimator

Importantly the separable mode expansion allows us not only to measure $f_{\text{NL}}^{\text{th}}$ efficiently for any given theoretical bispectrum, but it also allows us to reconstruct the full bispectrum in a model-independent manner by measuring a set of independent f_{NL} 's and summing up the corresponding contributions to the bispectrum [26, 27]. To see this, note that the transformation $R_n = \sum_m \lambda_{nm} Q_m$ implies $\alpha_n^Q = \sum_p \lambda_{pn} \alpha_p^R$ and from $\langle R_n, R_m \rangle_{\text{noweight}} = \delta_{nm}$ we get $\gamma = \lambda^{-1}(\lambda^{-1})^T$. Plugging this into (45) gives

$$\hat{f}_{\text{NL}}^{\text{th}} = \frac{1}{N_{\text{th}}} \sum_m \alpha_m^R \beta_m^R, \quad (52)$$

with

$$\beta_m^R \equiv (2\pi)^3 \sum_n \lambda_{mn} \int d^3\mathbf{x} [M_r M_s M_t - 3\langle M_{\{r} M_s \} M_t \rangle], \quad (53)$$

where the index n labels the combination r, s, t . If $B_\delta^{\text{th}} = \langle B_\delta^{\text{obs}} \rangle$ then (46) becomes

$$\langle \hat{f}_{\text{NL}}^{\text{th}} \rangle = \frac{1}{N_{\text{th}}} \sum_m \alpha_m^R \alpha_m^R. \quad (54)$$

Equations (52) and (54) imply

$$\langle \beta_n^R \rangle = \alpha_n^R. \quad (55)$$

Therefore we can estimate the full bispectrum with [26, 27]

$$\hat{B}_\delta(k_1, k_2, k_3) = \sum_{n=0}^{n_{\text{max}}-1} \beta_n^R B_n^R(k_1, k_2, k_3), \quad (56)$$

where B_n^R is given by (51). Intuitively the coefficients β_n^R measure the components of the orthonormal basis bispectra B_n^R in the data and \hat{B}_δ measures the projection of the bispectrum on the subspace of bispectra spanned by the B_n^R .

This approach is extremely efficient with the calculation of each β_n^R coefficient being equivalent to a single 3D integration over products of fast Fourier transforms. While theoretically a complete basis would require N^3 modes in practice far fewer modes ($\mathcal{O}(50)$) are necessary to reconstruct the bispectrum accurately.

The primordial contribution to the matter bispectrum will be extracted by measuring the difference of the bispectrum between non-Gaussian and Gaussian initial conditions,

$$\hat{B}_{\text{NG}} = \sum_{n=0}^{n_{\text{max}}-1} [\beta_n^R - (\beta_n^R)_{\text{Gauss}}] B_n^R. \quad (57)$$

As will be discussed in more detail later, the difference is computed seed by seed to reduce error bars.

The time-dependence of the expansion coefficients α_n^R and the β_n^R coefficients can be read off from (44) to be $(\alpha_n^R)_{\text{grav}} \propto D(z)$ for the gravitational bispectrum and $(\alpha_n^R)_{\text{NG}} \propto D(z)^0$ for primordial bispectra, assuming tree level perturbation theory where $P_\delta \propto D^2(z)$. In practice we must use the nonlinear power in (44) and (47) implying slightly different time dependences for α_n^R in the nonlinear regime (see e.g. the middle panel of Fig. 14a, which will be discussed in more detail later).

Fast modal bispectrum correlations

To analyse the reconstructed bispectrum and to control the accuracy of the separable method, the following shape correlations are computed using (39):

$$\mathcal{C}_{\alpha,\text{th}} \equiv \mathcal{C} \left(\sum_n \alpha_n^R B_n^R, B_\delta^{\text{th}} \right) = \sqrt{\frac{\sum_n (\alpha_n^R)^2}{\langle B_\delta^{\text{th}}, B_\delta^{\text{th}} \rangle}}, \quad (58)$$

$$\mathcal{C}_{\beta,\alpha} \equiv \mathcal{C} \left(\langle \hat{B}_\delta \rangle_{\text{sim}}, \sum_n \alpha_n^R B_n^R \right) = \frac{\sum_n \alpha_n^R \langle \beta_n^R \rangle_{\text{sim}}}{\sqrt{\sum_m (\alpha_m^R)^2 \sum_p \langle \beta_p^R \rangle_{\text{sim}}^2}}, \quad (59)$$

$$\mathcal{C}_{\beta,\text{th}} \equiv \mathcal{C} \left(\langle \hat{B}_\delta \rangle_{\text{sim}}, B_\delta^{\text{th}} \right) = \mathcal{C}_{\beta,\alpha} \mathcal{C}_{\alpha,\text{th}}. \quad (60)$$

Here $\langle \hat{B}_\delta \rangle_{\text{sim}}$ denotes the average of (56) over independent simulations and we truncate all sums appearing in the above expressions and in (56) after n_{max} modes. The first shape correlation measures how well the separable expansion (44) of the theoretical bispectrum approximates the theoretical bispectrum. The second shape correlation quantifies how well the estimated bispectrum $\langle \hat{B}_\delta \rangle_{\text{sim}}$ agrees with the separable expansion of the theoretical bispectrum. The product of these two shape correlations gives the shape correlation between the reconstructed bispectrum and the theoretical bispectrum.

Cumulative measures of non-Gaussianity

Additionally to these shape correlations we will also compare the projections (52) of the measured bispectrum on theory bispectra, as well as the cumulative signal to

noise of the average reconstructed bispectrum, which can be expressed in terms of the measured average $\langle \beta_n^R \rangle_{\text{sim}}$ as⁸

$$\| \langle \hat{B}_\delta \rangle_{\text{sim}} \| = \sqrt{\frac{\sum_n \langle \beta_n^R \rangle_{\text{sim}}^2}{6(2\pi)^3}}, \quad \bar{F}_{\text{NL}}^{\text{sim}} = \sqrt{\frac{\sum_n \langle \beta_n^R \rangle_{\text{sim}}^2}{N_{B_\delta^{\text{prim,loc}}}}}. \quad (61)$$

The norm was defined in (40) using the cumulative signal to noise squared of the bispectrum. As a consistency check we check if (61) also measures the cumulative signal to noise squared of the β_n^R coefficients. The theoretical covariance of β_n^R involves the 6-point function of the density perturbation. Taking only the Gaussian contribution into account and assuming that different Fourier modes are uncorrelated we find

$$\langle \beta_n^R \beta_m^R \rangle = 6(2\pi)^3 \delta_{nm}. \quad (62)$$

This predicts $\sigma_{\beta_n^R} = \sqrt{6(2\pi)^3}$ for Gaussian simulations and therefore confirms that (61) measures the cumulative signal to noise of the reconstructed bispectrum. We confirmed the prediction for $\sigma_{\beta_n^R}$ quantitatively in Gaussian simulations, but we have not assessed non-Gaussian corrections to the predicted noise (see e.g. [59]). Note that our plots show 1σ sample standard deviations obtained by running realisations with different random number seeds.

Towards experimental setups

For the bispectrum measurements presented below we will drop the second term in the square brackets in (53), i.e. we assume that different modes of the density perturbation are uncorrelated, $\langle \delta_{\mathbf{k}} \delta_{\mathbf{k}'} \rangle \propto \delta_D(\mathbf{k} + \mathbf{k}')$, which is true for a statistically homogeneous field. In experimental setups, which are not considered here, off-diagonal mode couplings from inhomogeneous noise can be incorporated in (53) with the linear term $\langle MM \rangle M$, without affecting the efficiency of the bispectrum estimator (56). Ref. [59] explores how modifications to the denominator of the estimator (34) in presence of off-diagonal mode couplings can be incorporated efficiently with modal expansions and an implementation for CMB experiments has been developed successfully.

Comparison to other bispectrum estimators

An alternative way to reconstruct the bispectrum is to estimate the three-point correlation function directly,

⁸ Alternatively using $(\sum_n \langle \beta_n^R \rangle_{\text{sim}}^2)_{\text{sim}}$ would add undesirable contributions from the variances of the β_n^R , which become relevant if the measurements are not signal-dominated.

taking a subset of all possible triangle configurations that yields the desired accuracy of the bispectrum [12, 14, 25]. In contrast our estimator takes all possible triangle configurations into account in a very efficient way, so that the bispectrum can be measured on the complete range of scales that were included in the N -body simulation. For example, with our method the extraction of the bispectrum of a 1024^3 grid takes about one hour on 6 cores, which is only a small fraction of the time required to run an N -body simulation of this size. Moreover our estimator compresses the information about the shape of the bispectrum, which is a function of the whole three-dimensional tetrahedral domain allowed by the triangle condition, to n_{\max} numbers β_n^R , where n_{\max} is the number of basis functions used in the expansion (44). This simplifies further processing of the bispectrum, e.g. for comparisons with theoretical models and for obtaining fitting formulae. Once β_n^R is measured from the data, we can not only obtain the full bispectrum with (56), but we can also calculate full three-dimensional shape correlations, the cumulative signal to noise and the nonlinearity parameter $f_{\text{NL}}^{\text{th}}$ associated to any theoretical bispectrum B_δ^{th} without additional computational cost, using (59), (61) and (52), respectively. In presence of inhomogeneous noise we can in principle include off-diagonal covariance elements $\langle \delta_{\mathbf{k}} \delta_{\mathbf{k}'} \rangle$ in a straightforward way. Finally our approach allows us to estimate the trispectrum efficiently [26], which has been shown for a class of trispectrum shapes in [27] (see also [4, 9]), but we leave the application to N -body simulations for future work.

Bispectrum visualisation

Often in the literature the bispectrum is visualised by plotting one- or two-dimensional slices through the tetrapyd shown in Fig. 1. E.g. the plots in [58] correspond to two-dimensional slices through the tetrapyd obtained by varying k_2 and k_3 at fixed k_1 and removing the $k_3 > k_2$ part of the slice by symmetry. Some plots in [7] and in this paper show two-dimensional tetrapyd slices with $k_1 + k_2 + k_3 = \text{const}$. While such slices are sufficient for scale-invariant primordial bispectra, late time bispectra typically have different triangle dependences at different overall scales $k_1 + k_2 + k_3$. This motivates plotting late time bispectra on the full three-dimensional tetrapyd instead of plotting particular slices through the tetrapyd.

Instead of the unweighted bispectrum the so-called reduced bispectrum $Q \equiv B_\delta / (P_\delta(k_1)P_\delta(k_2) + 2\text{perms})$ is often shown, because it reduces the dynamical range of the bispectrum and for the tree level gravitational contribution it is independent of time, overall scale and power spectrum normalisation and almost independent of cosmology [31]. Instead we will plot the signal to noise weighted bispectrum $\sqrt{k_1 k_2 k_3} / (P_\delta(k_1)P_\delta(k_2)P_\delta(k_3)) B_\delta$ because then the product of the shown functions gives

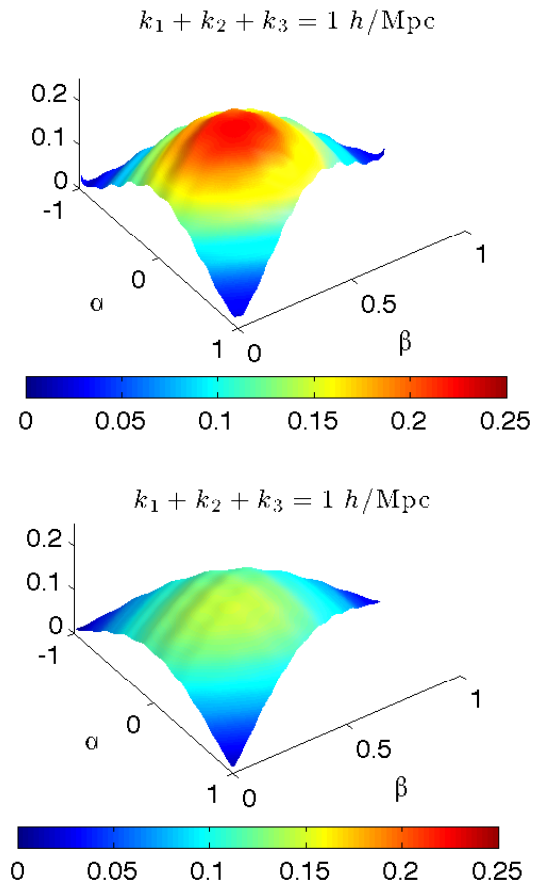


Figure 4. Bispectrum weights $[P_\delta(k_1)P_\delta(k_2) + 2 \text{ perms}]^{-1}$ (top) and $\sqrt{k_1 k_2 k_3} / [P_\delta(k_1)P_\delta(k_2)P_\delta(k_3)]$ (bottom) evaluated with CAMB [28] at redshift $z = 30$ on slices with $k_1 + k_2 + k_3 = 1 h/\text{Mpc}$.

the scalar product defined in (38) [58], visual similarity indicates a high shape correlation (39) and the dynamical range of the unweighted bispectrum is also greatly reduced, which is of advantage for plotting purposes. For linearly evolved primordial bispectra (24), the signal to noise weighted bispectrum is time-independent in the linear regime.

Qualitatively the two weights are quite similar in the regime relevant for most plots of this paper, see Fig. 4. However they differ in the squeezed limit, because for decreasing k_1 , $P_\delta(k_1)P_\delta(k_2)$ turns over at $k_1 = k_{\text{eq}}$, whereas $\sqrt{P_\delta(k_1)P_\delta(k_2)P_\delta(k_3)} / (k_1 k_2 k_3)$ turns constant where $P(k_1)/k_1$ turns constant, which is on somewhat larger scales than k_{eq} . While it is not straightforward to deduce the squeezed limit of an unweighted bispectrum from a plot of its weighted form, one can compare plots of different bispectra if they are weighted in the same way to deduce the relative behavior in the squeezed limit.

V. SIMULATION SETUP, INITIAL CONDITIONS AND VALIDATION

N-body simulations setup

We use the separable mode expansion method described in [26, 27] to generate realisations of the initial primordial potential $\Phi = -3\mathcal{R}/5$ during matter domination with the desired primordial power spectrum and bispectrum. For 512^3 particles this takes about 10 minutes per seed on one core and works for separable as well as non-separable bispectra, therefore being more general than other proposed methods [23, 25]. From Φ we calculate the linear density perturbation δ at the initial redshift of the simulation with the Poisson equation (2). We then use this initial density perturbation to displace the initial particles from an unperturbed distribution with the 2LPT method [60, 61], which also determines the initial particle velocities. Then the *N*-body code Gadget-3 [62, 63] simulates the time evolution until today and we use a cloud in cell scheme to calculate the density perturbation δ of the particle distribution on a grid at different redshifts. After deconvolving δ with the cloud in cell kernel we compute the power spectrum P_δ and the coefficients β_n^R from (53) using $n_{\max} = 50$ modes. Finally we reconstruct the full bispectrum with (56) and calculate its norm \hat{F}_{NL} (61) as well as its shape correlation $\mathcal{C}_{\beta,\alpha}$ (59) with theoretical bispectra and its nonlinear amplitude (52).

Table I lists the parameters of the *N*-body simulations that were performed in this work. All simulations assume a flat Λ CDM model with the WMAP-7 [1] parameters $\Omega_b h^2 = 0.0226$, $\Omega_c h^2 = 0.11$, $\Omega_\Lambda = 0.734$, $h = 0.71$, $\tau = 0.088$, $\Delta_{\mathcal{R}}^2(k_0) = 2.43 \times 10^{-9}$ and $n_s(k_0) = 0.963$, where $k_0 = 0.002\text{Mpc}^{-1}$. Note that the primordial power spectrum is given by $P_\Phi(k) = (9/25) (2\pi^2/k^3) \Delta_{\mathcal{R}}^2(k_0) (k/k_0)^{n_s-1}$.

Regular grid vs glass initial conditions

For the unperturbed particle distribution, from which initial particles are displaced using the 2LPT method, we either use a regular grid or a glass configuration, which is obtained by placing particles randomly in the box and then evolving them with the sign of gravity flipped in Gadget-3 [63, 64]. A disadvantage of glass initial conditions is that they require generating a glass and specifying when the glass configuration has converged (see e.g. [65] for a discussion). In contrast, regular grid initial conditions are easier to set up but break statistical isotropy, which may have implications for structure formation. We will compare the different initial condition setups first for Gaussian and then non-Gaussian initial conditions.

Name	NG shape	f_{NL}	$L[\frac{\text{Mpc}}{h}]$	N_p	z_i	$L_s[\frac{\text{kpc}}{h}]$	N_r	glass
G512g	–	–	1600	512	49	156	3	yes
G512	–	–	1600	512	49	156	3	no
G_L^{512}	–	–	{400, 100}	512	49	{39, 9.8}	3	no
G768	–	–	2400	768	19	90	3	no
G1024	–	–	1875	1024	19	40	2	no
Loc10g	local	10	1600	512	49	156	3	yes
Loc10	local	10	1600	512	49	156	3	no
Loc10_L^{512}	local	10	{400, 100}	512	49	{39, 9.8}	3	no
Loc10^-	local	–10	1600	512	49	156	3	no
Loc20	local	20	1600	512	49	156	3	no
Loc50	local	50	1600	512	49	156	3	no
Eq100g	equil	100	1600	512	49	156	3	yes
Eq100	equil	100	1600	512	49	156	3	no
Eq100_L^{512}	equil	100	{400, 100}	512	49	{39, 9.8}	3	no
Eq100^-	equil	–100	1600	512	49	156	3	no
Orth100g	orth	100	1600	512	49	156	3	yes
Orth100	orth	100	1600	512	49	156	3	no
$\text{Orth100}_{400}^{512}$	orth	100	400	512	49	39	3	no
Orth100^-	orth	–100	1600	512	49	156	3	no
Flat10	flat	10	1600	512	49	156	3	no
$\text{Flat10}_{400}^{512}$	flat	100	400	512	49	39	3	no

Table I. Parameters of *N*-body simulations: Non-linearity parameter f_{NL} , box size L , number of particles per dimension N_p , initial redshift of the simulations z_i , softening length L_s and number of realisations (i.e. random seeds) N_r for each parameter set. ‘glass’ indicates if the initial particles were displaced from a regular grid or from a glass configuration. Initial conditions for non-local non-Gaussian simulations were generated with the separable method described in [26, 27]. All simulations use 2LPT [60, 61] to get the initial particle distribution, which is then evolved with Gadget-3 [62, 63].

Measured bispectra for Gaussian *N*-body simulations will be shown in Fig. 14 in Section VI. Simulations started from glass and regular grid initial conditions are shown in Fig. 14a and Fig. 14b, respectively. At early times regular grid initial conditions produce a bispectrum which is more than three times as large as the tree level prediction. This significant spurious bispectrum is not present for glass initial conditions and must therefore be caused by the breaking of isotropy induced by the regular grid. Fig. 14b shows that the spurious bispectrum decays with time as the regular grid structure is washed out by the growing gravitational perturbations. At late times, $z \leq 3$, the bispectra from regular grid and glass initial conditions differ by at most 10% in their cumulative signal to noise and by less than 0.5% in their shape correlation to the tree level prediction, see Fig. 14c.

We conclude that at the 10% accuracy level (for Gaussian simulations with $L = 1600\text{Mpc}/h$, 512^3 particles and $k_{\max} = 0.5h/\text{Mpc}$), both glass and regular grid initial conditions can be used to extract the gravitational bis-

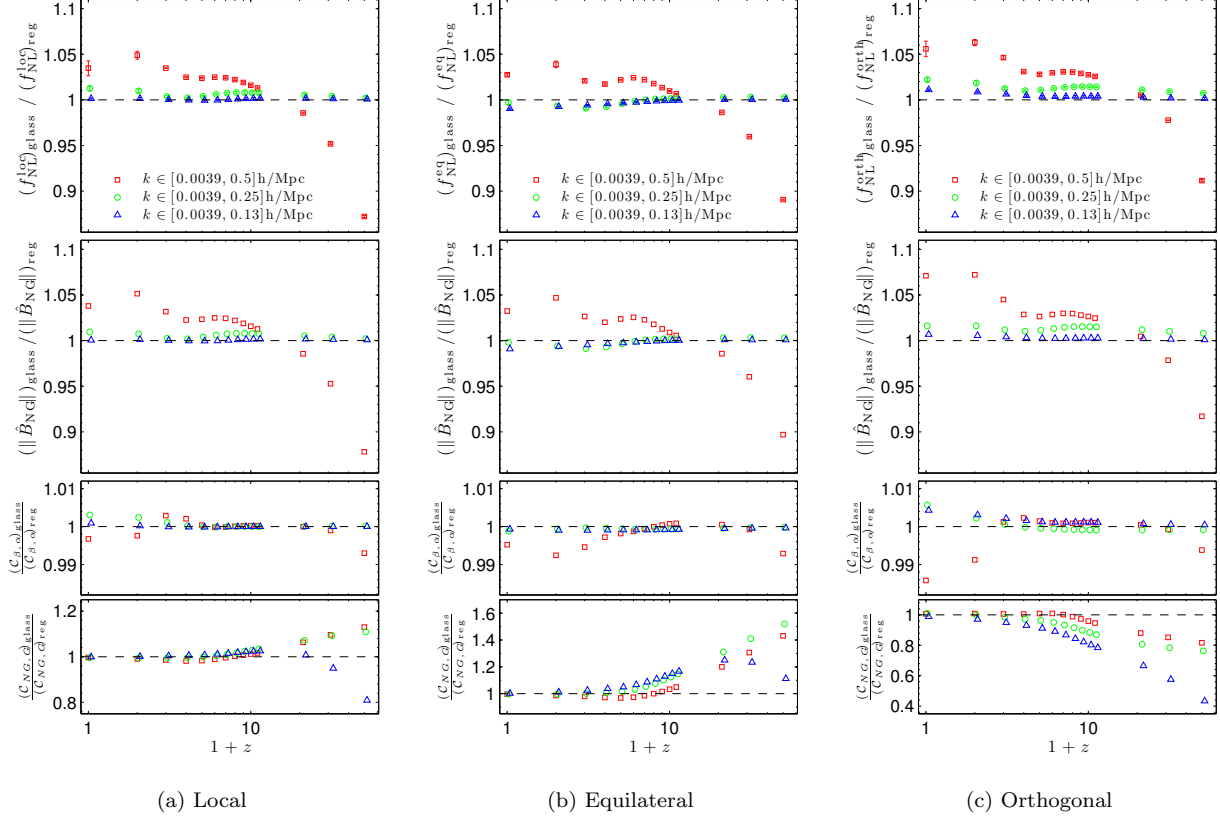


Figure 5. Impact of glass initial conditions on measured non-Gaussian bispectra in simulations Loc10, Eq100 and Orth100. We plot the ratio to simulations with regular grid initial conditions. The top panel contains error bars obtained by calculating the sample standard deviation of the ratio for each seed. We do not show error bars in the other panels because they depend on $\sum_n \langle \beta_n^R \rangle_{\text{sim}}^2$ and are therefore more difficult to estimate. However they should be similar to the errors in the top panel because of (43). The large deviations in the bottom panel are mainly due to the different gravitational bispectra for glass and regular grid initial conditions as shown in Fig. 14c.

spectrum from Gaussian simulations as long as the bispectrum is measured at low redshifts when the regular grid is washed out. The difference between regular grid and glass initial conditions decreases when reducing the cut-off k_{max} used for the bispectrum estimation because then structures of the size of the grid separation are smoothed out.

For non-Gaussian simulations, Fig. 5 shows how glass initial conditions change the non-Gaussian excess bispectrum \hat{B}_{NG} (57) compared to regular grid initial conditions. At $z \leq 10$ the shape of \hat{B}_{NG} is consistent between glass and regular grid initial conditions at the 1.5% level for the simulations Loc10, Eq100 and Orth100. However, the total integrated bispectrum \bar{F}_{NL} differs by up to 7% for $z \leq 10$. At earlier times the deviations are somewhat larger. Compared to the full gravitational bispectrum for Gaussian initial conditions shown in Fig. 14a, the impact of glass initial conditions on \hat{B}_{NG} is quite small, possibly because the spurious bispectrum due to the regular grid is partly subtracted out when calculating $\hat{B}_{\text{NG}} = \hat{B} - \hat{B}_{\text{Gauss}}$.

Whether regular grid or glass initial conditions are rep-

resenting the statistics of the non-Gaussian density perturbation more successfully is not unambiguous. Regular grid initial conditions introduce a spurious contribution to the full bispectrum \hat{B} at early times, which can be avoided using glass initial conditions. However glass initial conditions represent the primordial contribution \hat{B}_{NG} slightly less accurately than regular grid initial conditions at the starting redshift of the simulation. However these effects impact \hat{B}_{NG} only at the $\mathcal{O}(5\%)$ level at $z \leq 10$, so that both glass or regular grid initial conditions can be used at this level of precision. As for Gaussian simulations the two initial condition methods agree better when k_{max} is reduced (see Fig. 5) and grid discretization effects are minimized.

Validation and convergence tests

First we test the setup of the initial conditions and the N -body simulations by comparing the measured matter power spectrum with the power spectrum predicted by linear theory and by CAMB [28, 30] in Fig. 6. Next we

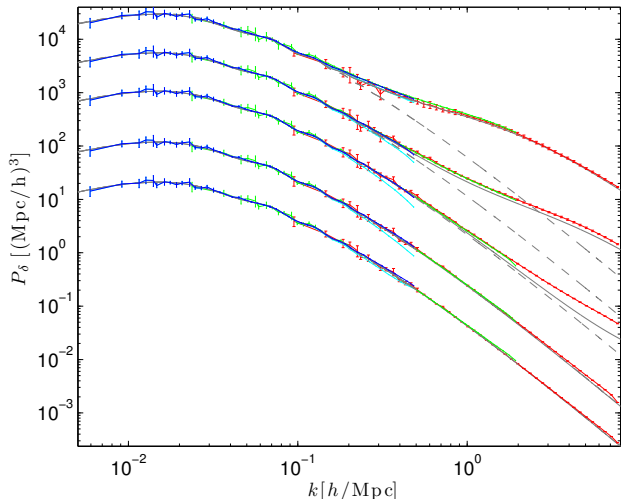


Figure 6. Measured matter power spectra in simulations G_{100}^{512} (red), G_{400}^{512} (green), G512 (blue) and G512g (cyan) in comparison with power from linear perturbation theory (grey dashed) and CAMB (grey solid, [28, 30]). See Table I for parameters. Curves from bottom to top correspond to redshifts $z = 49, 20, 6, 2, 0$.

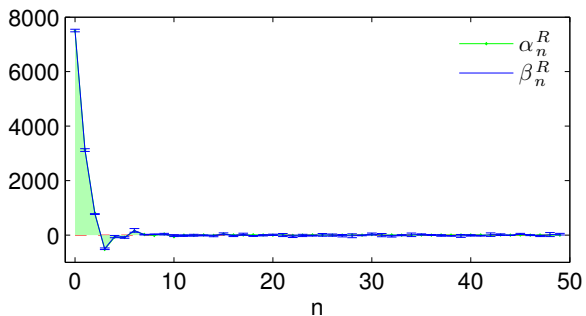


Figure 7. Shot noise validation test for the separable bispectrum estimator: Measured bispectrum coefficients β_n^R (53) (blue, averaged over 3 seeds) for 512^3 particles placed randomly in a $L = 1600\text{Mpc}/h$ box, compared with the expansion coefficients α_n^R (44) (green) for the expected pure shot noise bispectrum. The shape correlation is $\mathcal{C}_{\beta,\alpha} = 0.9998$. For better visibility the region under the α_n^R curve is colored green.

perform a simple test of the bispectrum estimator by distributing particles randomly in a box and comparing the measured bispectrum with the pure shot noise bispectrum $B_\delta^{\text{shot}} = L^6/N_p^6$ [66], see Fig. 7. These two tests show that the basic setup of the simulations is correct and that the separable bispectrum estimator works well.

To check convergence of the N -body simulations and the bispectrum measurements we compare results for box sizes $L = \{1600, 400, 100\}\text{Mpc}/h$ with $N_p^3 = 512^3$ particles. For each simulation we measure the bispectrum from $k_{\min} = 2\pi/L$ to $k_{\max} = \{1, 0.5, 0.25\} \times (\frac{N_p}{4} \frac{2\pi}{L})$ by

imposing a sharp k filter on the density perturbation $\delta_{\mathbf{k}}$.

The measured late time bispectra are shown in Fig. 8 as functions of k_{\max} . Data points with the same k_{\max} measured in a low and high resolution simulation can differ in the plots because, for these data, k_{\min} differs by a factor of 4 and, therefore, the number of modes for the bispectrum estimation differs by a factor of $4^3 = 64$, which affects particularly the cumulative signal to noise $\|\hat{B}\|$. In contrast the quantity \bar{F}_{NL}^B is normalised with respect to the linearly evolved local shape over the given range of scales and therefore takes differences in the number of modes into account. Thus the agreement of \bar{F}_{NL}^B (and $\mathcal{C}_{\beta,\alpha}$) for the different simulations seen in Fig. 8 shows that the N -body simulations have converged and the bispectrum estimator gives consistent results.

It should be noted that the shown cumulative signal to noise takes only Gaussian noise into account, c.f. (41). This simplification is not expected to be valid in the strongly nonlinear regime so that the correct signal to noise may differ significantly. However to assess this issue in a robust manner we need to run more realisations of the N -body simulations or use larger boxes with more particles.

Error bars

To obtain error bars for quantities based on the primordial contribution to the bispectrum, we use seed by seed subtracted coefficients $\langle \beta_m^R - (\beta_m^R)_{\text{Gauss}} \rangle_{\text{sim}}$ and calculate their sample standard deviations, which are then used for standard error propagation assuming uncorrelated β_m^R . The error bars therefore measure how much the primordial contribution to the matter bispectrum scatters for different seeds of the initial Gaussian field Φ_G in the simulations. Compared to calculating the difference between the average bispectra, $\langle \beta_m^R \rangle_{\text{sim}} - \langle (\beta_m^R)_{\text{Gauss}} \rangle_{\text{sim}}$, the seed by seed subtraction reduces the error bars, because the late time bispectra for Gaussian and non-Gaussian initial conditions are very correlated due to the presence of the large gravitational bispectrum in both cases.

In real observations we do not know the realisation of our universe with perfectly Gaussian initial conditions and therefore error bars will be larger if we measure $\beta_m^R - \langle (\beta_m^R)_{\text{Gauss}} \rangle_{\text{sim}}$. We do not discuss the interesting issue of observability of primordial non-Gaussianity here, because instead of dark matter bispectra this requires halo bispectra, which we leave for future work (but see [17] for the local shape).

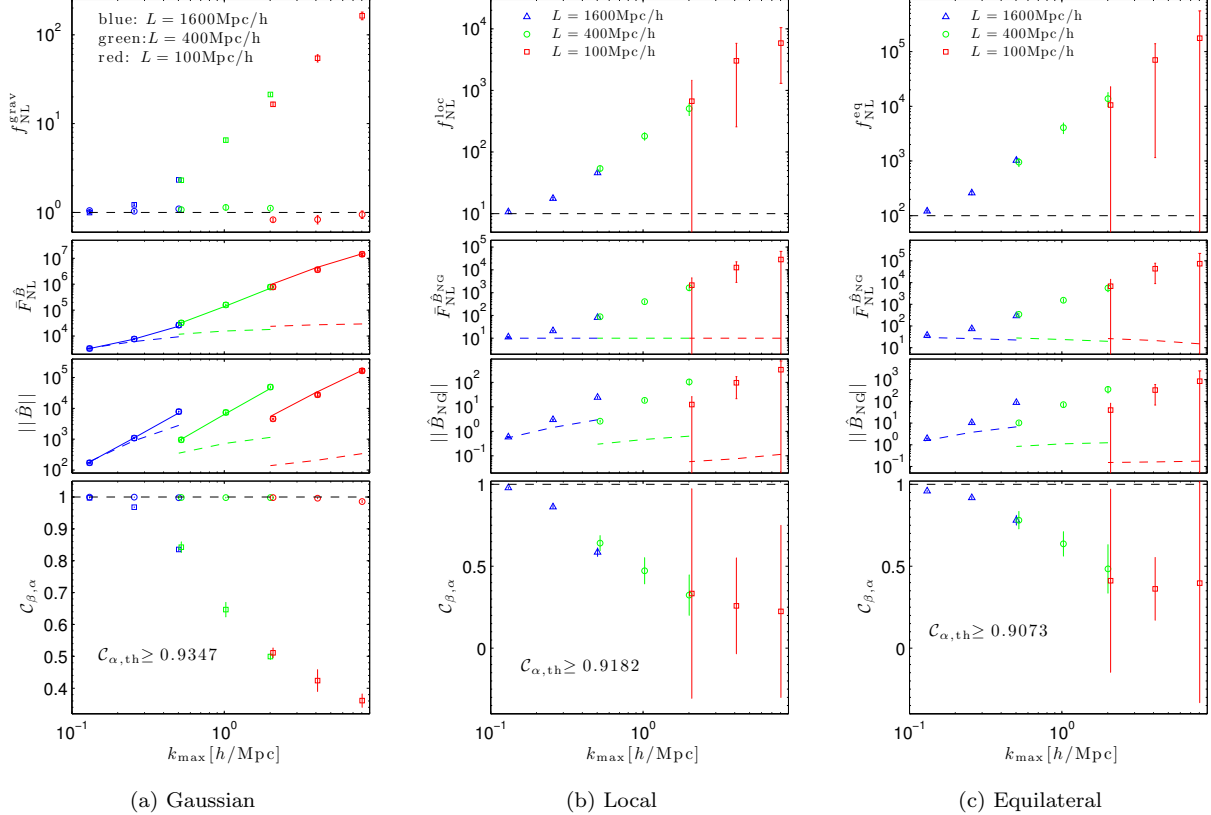


Figure 8. Convergence tests: Dependence of measured bispectra on k_{\max} at $z = 0$ for simulations with 512^3 particles and box sizes $L = \{1600, 400, 100\}$ Mpc/h (G512, $G_{\{400,100\}}^{512}$, Loc10, $\text{Loc10}_{\{400,100\}}$, Eq100 and $\text{Eq100}_{\{400,100\}}$). (a) *Top panel*: Projection of measured bispectrum on the tree level prediction (7) (squares) and on the fitting formula from [14] (circles). *Middle panels*: Cumulative signal to noise of measured bispectrum (squares/circles), tree level prediction (7) (dashed lines) and fitting formula from [14] (solid lines). *Bottom panel*: Shape correlation of measured bispectrum with tree level prediction (squares) and fitting formula from [14] (circles). (b-c) Measured non-Gaussian bispectra \hat{B}_{NG} (57) in simulations with local and equilateral initial conditions compared to the linearly evolved primordial bispectrum (24) (dashed lines). Note comments on the cumulative signal to noise on small scales in the main text.

VI. GRAVITATIONAL BISPECTRUM RESULTS

Gravitational collapse and bispectrum evolution

The cosmic web simulated by N -body simulations has a complex filamentary structure, which is illustrated in Fig. 9a. The bispectrum of this dark matter distribution is shown in Fig. 9b. In the following we will discuss how the bispectrum can be used as a quantitative tool to characterise the structures formed by gravitational collapse and to study modifications due to primordial non-Gaussianity. We will demonstrate the unbiasedness of our bispectrum estimator by comparison with perturbation theory for large scales at early times.

We can develop a qualitative and visual understanding of the bispectrum by comparing it to the form of large-scale structures. Fig. 10 shows snapshots of the dark matter distribution at redshifts $z = 4, 2$ and 0 on the left and the corresponding measured bispectrum signal on the right. It is apparent that the shape of the bispec-

trum characterises the three-dimensional structures that have formed. The diffuse blob- and pancake-like structures at early times, $z = 4$, correspond to a flattened bispectrum, which peaks at the edges of the tetrapyd and is predicted by leading order perturbation theory. At later times we find that filaments and clusters induce a bispectrum with a relatively enhanced signal for equilateral triangle configurations, as expected from sections II and III. As illustrated in Fig. 11, the bispectrum signal shows a similar transition for varying overall scale $k_1 + k_2 + k_3$ at fixed time $z = 0$, which indicates self-similar behaviour.

Comparison with leading order PT

On large scales and at early times we expect the gravitational bispectrum to agree with leading order perturbation theory (7). To test this Fig. 12a shows the β_n^R coefficients (53) measured in the Gaussian N -body simulations G512 with $L = 1600$ Mpc/h in comparison with

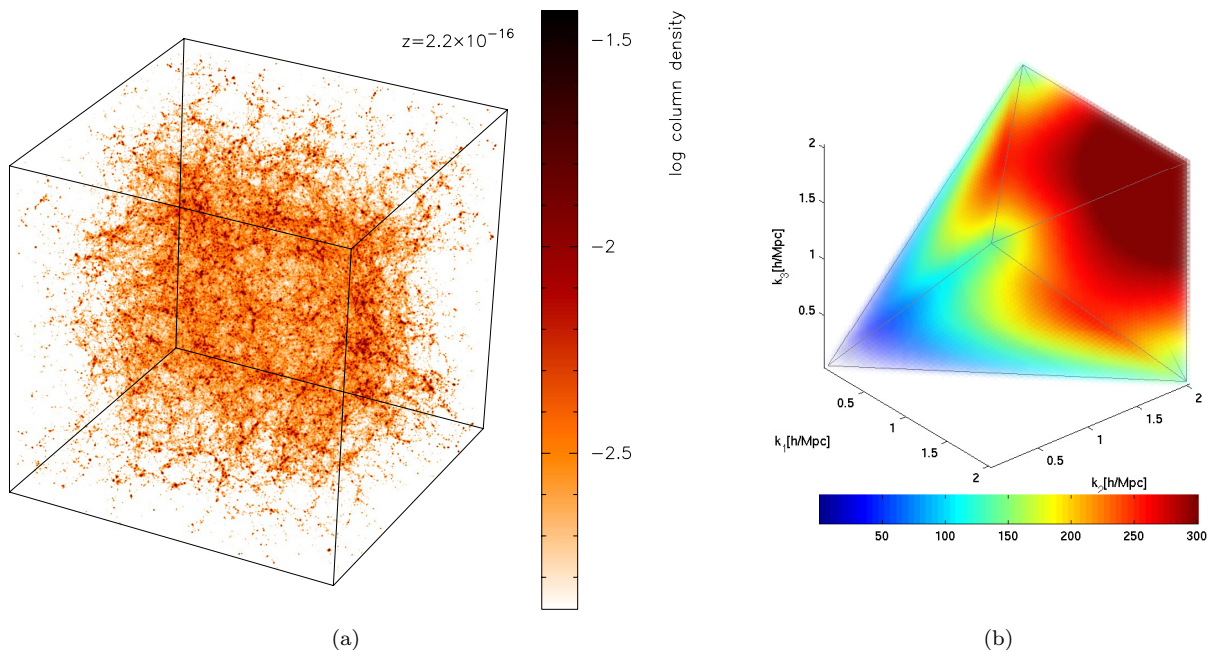


Figure 9. (a) Dark matter distribution in one of the G_{400}^{512} simulations of 512^3 particles in a box with $L = 400\text{Mpc}/h$ at redshift $z = 0$. (b) Measured (signal to noise weighted) bispectrum in the range $0.016h/\text{Mpc} \leq k \leq 2h/\text{Mpc}$, averaged over the simulation on the left and two additional seeds. The opaqueness of the plotted points reflects the absolute value of the bispectrum.

the expansion coefficients α_n^R (44) of the tree level gravity bispectrum (7). The corresponding theoretical and estimated bispectra (56) are plotted over the full tetrapyd in Fig. 3 for $z = 30$ and Fig. 13 for $z = 2$ and $z = 0$. At early times, $z = 30$, the bispectrum agrees with tree level perturbation theory (7), which predicts that the signal to noise weighted bispectrum is large for folded and elongated configurations but is suppressed in the squeezed limit. However at $z = 0$ for $k \gtrsim 0.25h/\text{Mpc}$ the N -body bispectrum has an enhanced amplitude for elongated configurations and an additional equilateral contribution not captured by tree level perturbation theory, which breaks down on these scales as expected.

To analyse the measured bispectrum more quantitatively and to illustrate its time and scale dependence we show in Fig. 14 the measured amplitude $f_{\text{NL}}^{\text{grav}}$ of the gravitational bispectrum, its cumulative signal to noise $\|\hat{B}\|$ (40) and the cumulative signal to noise normalised to the local shape \hat{F}_{NL} (42), as well as the shape correlation \mathcal{C} (39) of the measured bispectra with the theoretical expectation. The meaning of these quantities is illustrated in Fig. 14f. We plot them as functions of redshift z and use different colors for different k ranges used for the bispectrum measurements. Note that $f_{\text{NL}}^{\text{grav}}$ is the amplitude of the gravitational bispectrum (7), i.e. tree level perturbation theory predicts $f_{\text{NL}}^{\text{grav}} = 1$ in this convention.

Fig. 14a and Fig. 14b show that for $0.0039h/\text{Mpc} \leq k \leq 0.5h/\text{Mpc}$ at $z = 0$ the tree level bispectrum underpredicts the total integrated bispectrum \hat{F}_{NL} by a factor of 2.8 and its shape correlation with the measured bis-

pectrum drops to 0.84, implying that the projection of the measured bispectrum on the tree level bispectrum is $f_{\text{NL}}^{\text{grav}} = 2.3$. At larger scales the tree level bispectrum describes the measured bispectra much more accurately until late times, as expected. Similar plots for Gaussian N -body simulations with 768^3 and 1024^3 particles are shown in Fig. 14d and Fig. 14e, demonstrating again the expected break down of tree level perturbation theory on small scales at late times.

Fitting formulae for Gaussian simulations

Separable polynomial expansion

The separable mode expansion allowed us to compress the measured N -body dark matter bispectra to $n_{\text{max}} = 50$ numbers β_n^R at each redshift. The first ten of these coefficients are listed in Table II and can be used as a polynomial fitting formula of the matter bispectrum by evaluating (56). The orthogonal contributions B_n^R appearing in (56) were defined in (51) and contain the nonlinear power spectrum P_δ as well as the orthogonal polynomials R_n , which can be obtained from Q_n , defined in (48), by the basis change⁹ $R_n = \sum_m \lambda_{nm} Q_m$.

⁹ The transformation matrix λ can be obtained from the authors upon request.

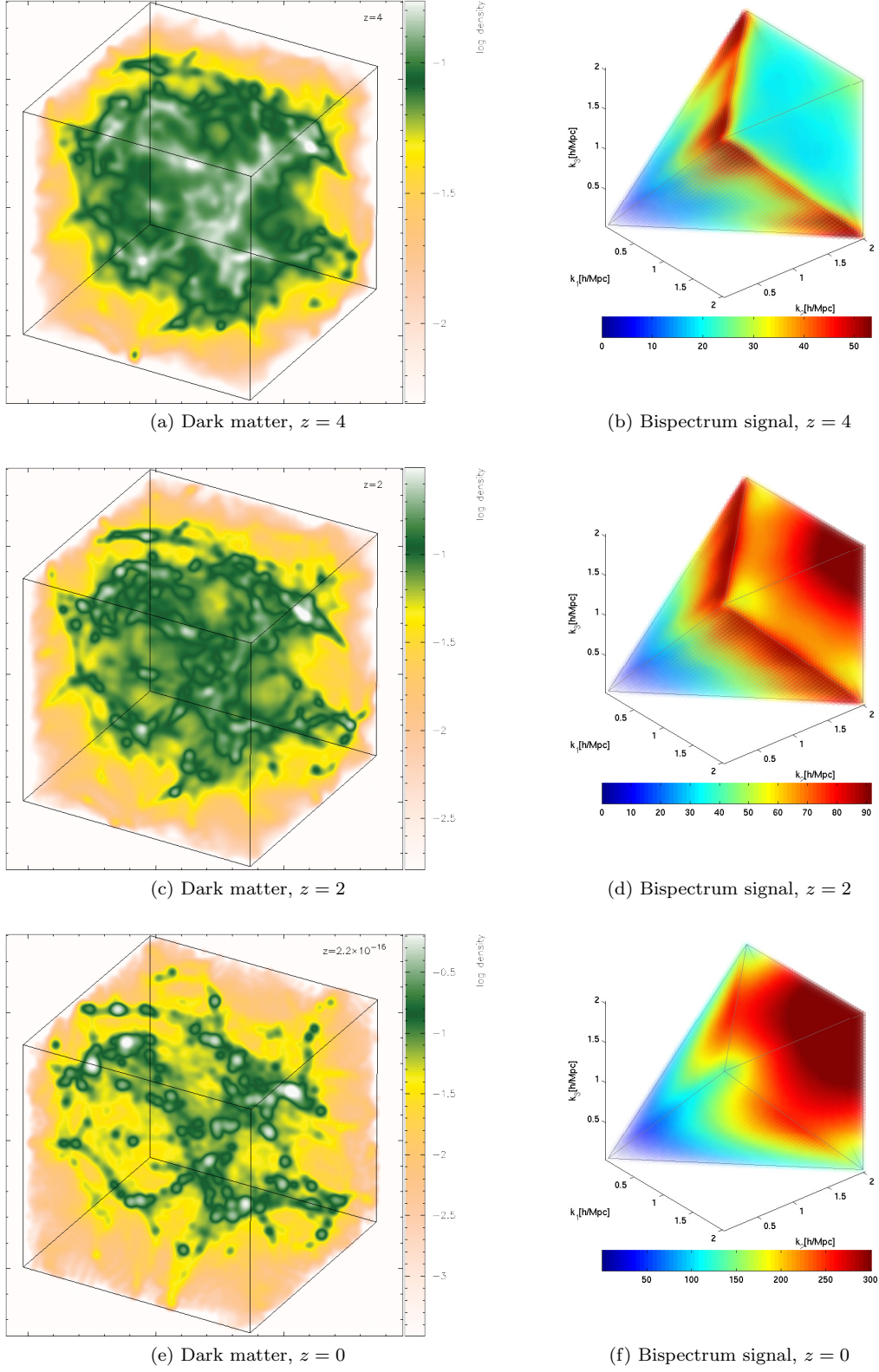


Figure 10. *Left*: Dark matter distribution in a $(40\text{Mpc}/h)^3$ subbox of one of the G_{400}^{512} simulations at redshifts $z = 4, 2$ and 0 , from top to bottom. *Right*: Measured (signal to noise weighted) bispectrum in the range $0.016h/\text{Mpc} \leq k \leq 2h/\text{Mpc}$, averaged over the simulation on the left and two additional seeds.

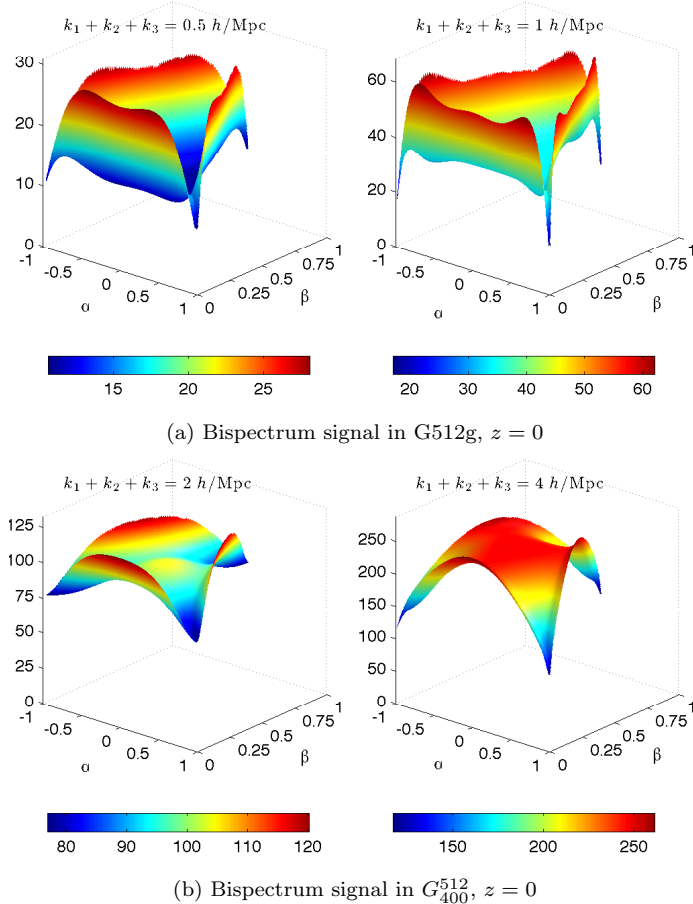


Figure 11. Bispectrum slices at fixed redshift $z = 0$ for different overall wavenumbers $k_{\text{sum}} = k_1 + k_2 + k_3$. For $k_{\text{sum}} \leq 1h/\text{Mpc}$ (upper row) the bispectrum signal dominates for flattened configurations, while an enhanced equilateral contribution clearly emerges for $k_{\text{sum}} = 2h/\text{Mpc}$ (bottom left). For $k_{\text{sum}} = 4h/\text{Mpc}$ (bottom right) the signal is large for all triangle configurations away from the squeezed limit, that is, it is nearly constant. The slices show signal to noise weighted bispectra measured in Gaussian simulations (a) G512g and (b) G_{400}^{512} .

The polynomials Q_n were sorted with the slice ordering defined in Eq. (58) of [8].

Time-shift model fit

We find a remarkably accurate fit to the matter bispectrum for Gaussian initial conditions by combining the modified tree level gravity shape $B_{\delta, \text{NL}}^{\text{grav}}$, defined in (8), with the ‘constant’ model $B_{\delta, \text{const}}^{\text{grav}}$, defined in (14), which approximates the 1-halo shape, that is,

$$B_{\delta}^{\text{fit}}(k_1, k_2, k_3) \equiv B_{\delta, \text{NL}}^{\text{grav}} + B_{\delta, \text{const}}^{\text{grav}}, \quad (63)$$

with fitting parameters c_1 and n_h .

The combined shape (63) is dominated by the perturbative gravity bispectrum at early times and by the constant or (approximate) halo model prediction at late

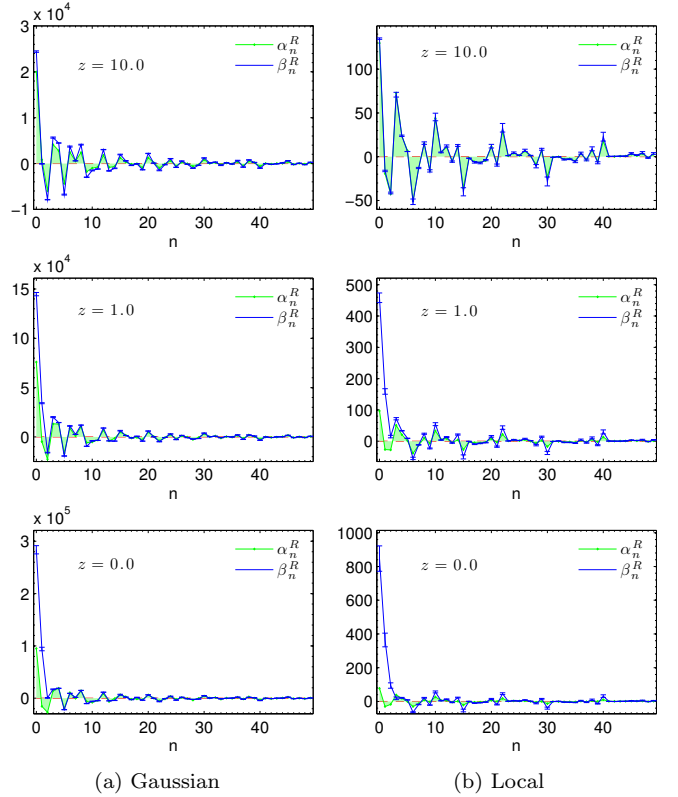


Figure 12. (a) β_n^R coefficients measured with (53) for the Gaussian simulations G512 compared to expansion coefficients α_n^R of the tree level gravitational bispectrum (7). (b) $\beta_n^R - (\beta_n^R)_{\text{Gauss}}$ measured in Loc10 simulations with $f_{\text{NL}}^{\text{loc}} = 10$ compared to α_n^R coefficients of the linearly evolved local shape (see (24) and (31)). β 's were calculated using all modes $\delta_{\mathbf{k}}$ with $0.0039h/\text{Mpc} \leq k \leq 0.5h/\text{Mpc}$. For better visibility the region under the α_n^R curves is colored green.

times. We will demonstrate that this combination can achieve a good fit of the matter bispectrum at all redshifts $z \leq 20$, while both the perturbative and the halo model prediction individually break down at intermediate redshifts, when nonlinearities are important but not all dark matter particles can be treated as residing in halos.

The fitting parameters c_1 and n_h in (14) are obtained as follows. At each measured redshift the arbitrary weight $w(z)$ in

$$B_{\delta}^{\text{opt}} = B_{\delta, \text{NL}}^{\text{grav}} + w(z)(k_1 + k_2 + k_3)^{\nu} \quad (64)$$

is analytically determined such that the correlation with the measured bispectrum $\mathcal{C}(\hat{B}_{\delta}, B_{\delta}^{\text{opt}})$ is maximal (see green lines in Fig. 15). Then c_1 and n_h are chosen such that $c_1 \bar{D}^{n_h}(z)$ approximates the optimal weight $w(z)$ over all redshifts (see black dashed lines in Fig. 15). Table III lists the fitting parameters obtained by this procedure.

The shape of the fitting formula (63) with the measured bispectrum is 99.8% or better at redshifts $z \leq 20$ for both $k_{\text{max}} = 0.5h/\text{Mpc}$ and $k_{\text{max}} = 2h/\text{Mpc}$

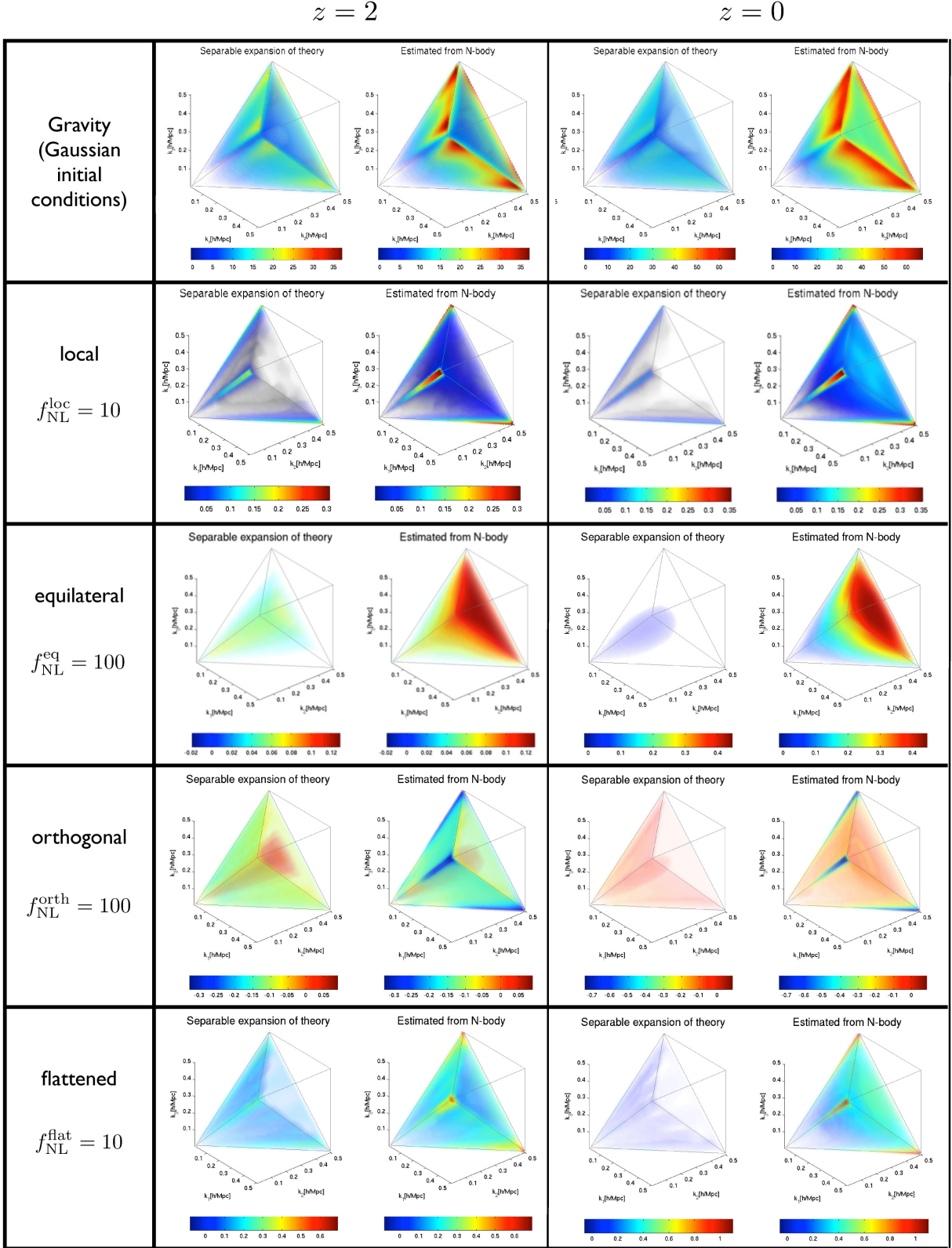


Figure 13. Comparison of measured N -body bispectra (56) (on the right in each black cell) with separable expansion of tree level theory (44) (on the left in each black cell) for simulations G512b, Loc10, Eq100, Orth100 and Flat10 at redshifts $z = 2$ and $z = 0$. The plot axes are $k_1, k_2, k_3 \leq 0.5h/\text{Mpc}$ and we plot signal to noise weighted bispectra $\sqrt{k_1 k_2 k_3 / (P_\delta(k_1) P_\delta(k_2) P_\delta(k_3))} B_\delta$ (see Fig. 3 for comparisons at $z = 30$ and further descriptions of the plots).

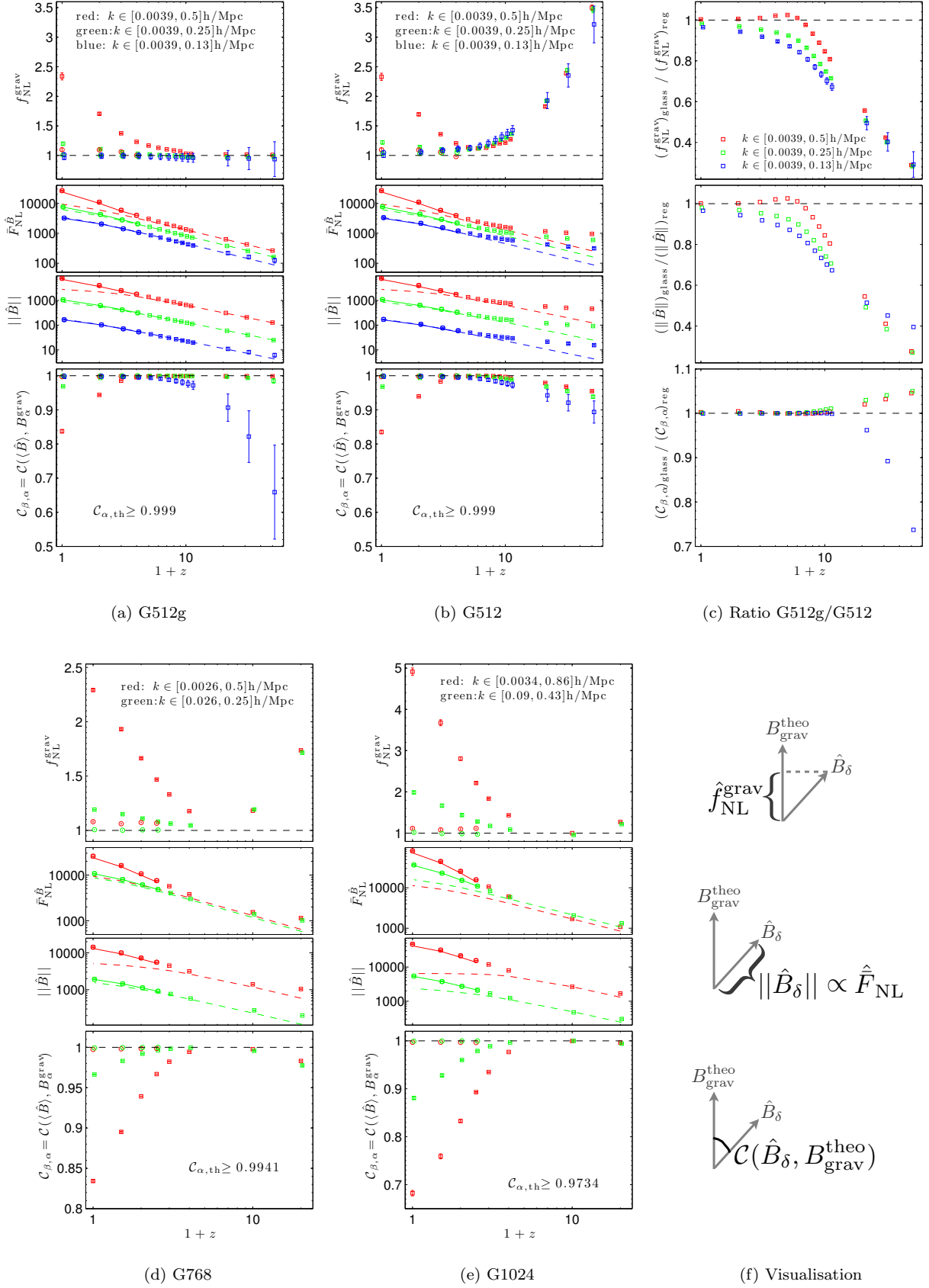


Figure 14. (a)-(e): Measured bispectra in *Gaussian* N -body simulations (see Table I) as a function of redshift. *Upper panels*: Amplitude $f_{\text{NL}}^{\text{grav}}$ of the tree level gravitational bispectrum (7) (squares), normalised to unity if the tree level prediction is correct, and amplitude of the fitting formula from [14] (circles). *Middle panels*: Total integrated bispectrum (61) of measured bispectrum (symbols), tree level prediction (dashed lines) and fitting formula by [14] (solid lines). *Lower panels*: Shape correlation (59) of reconstructed bispectrum with separable expansions of tree level theory (squares) and fitting formula from [14] (circles). Colors indicate different k ranges for the bispectrum estimation. The plotted quantities are visualised in (f).

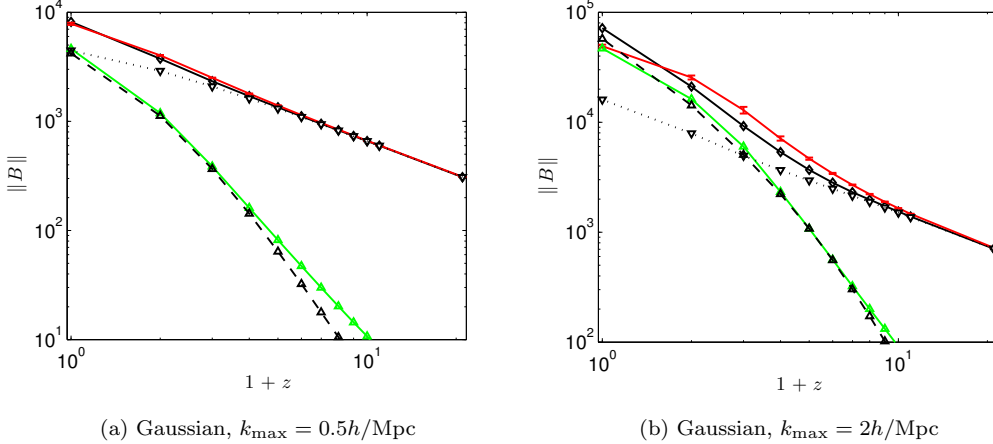
(a) Gaussian, $k_{\max} = 0.5h/\text{Mpc}$ (b) Gaussian, $k_{\max} = 2h/\text{Mpc}$

Figure 15. Motivation for using the growth function \bar{D} in the simple fitting formula (63). The arbitrary weight $w(z)$ in $B_{\delta}^{\text{opt}} = B_{\delta,\text{NL}}^{\text{grav}} + w(z)(k_1 + k_2 + k_3)^{\nu}$ is determined analytically such that $\mathcal{C}(\hat{B}_{\delta}, B_{\delta}^{\text{opt}})$ is maximal (for $\nu = -1.7$). We plot $\|B_{\delta,\text{NL}}^{\text{grav}}\|$ (black dotted), $\|w(z)(k_1 + k_2 + k_3)^{\nu}\|$ (green) and $B_{\delta,\text{const}}^{\text{grav}}$ (black dashed) as defined in (14) with fitting parameters given in Table III, illustrating that $w(z) = c_1 \bar{D}^{n_h}(z)$ is a good approximation. The continuous black and red curves show $\|B_{\delta}^{\text{fit}}\|$ from (63) and the estimated bispectrum size $\|\hat{B}_{\delta}\|$, respectively. The overall normalisation can be adjusted with N_{fit} as explained in the main text.

n	$\frac{(\beta_n^R)_{\text{G512}}}{1000}$	Loc10	Eq100	Orth100	Flat10	$\frac{(\beta_n^R)_{\text{G1875}}}{10000}$
0	283.8	846.8	3065	-793.5	3544	167
1	94.16	364.3	1390	-240.4	1484	63.06
2	0.6725	94.22	453	28.49	362.2	9.427
3	17.04	18.58	-183.5	-238.7	128.1	0.2799
4	18.89	21.7	-47.71	-173.6	163.5	5.774
5	-21.82	8.64	35.7	85.29	-43.72	-7.911
6	9.395	-63.53	-6.603	154.1	-232.5	1.329
7	1.624	-17.96	-2.818	53.24	-77.86	-0.4791
8	15.04	21.4	-57.18	-186	171.9	5.825
9	-10.25	-21.61	39.26	108.1	-109.2	-3.548

Table II. First 10 bispectrum expansion coefficients β_n^R from N -body simulations specified in Table I for $z = 0$. For simulations with non-Gaussian initial conditions we show the difference to the Gaussian simulation, $(\beta_n^R)_{\text{X}} = \beta_n^R - (\beta_n^R)_{\text{G512}}$. The shape correlation between the full measured bispectrum (56) for 50 modes and the bispectrum corresponding to the shown first 10 modes is 99.7%, 99.2%, 99.95%, 95.8%, 99.7% and 99.9% for the columns from the left to the right. We used $k_{\max} = 0.86h/\text{Mpc}$ for the G_{1875}^{1024} simulation in the column on the right and $k_{\max} = 0.5h/\text{Mpc}$ in all other columns.

as shown in the upper panels of Fig. 16. The model (63), therefore, contains all the meaningful bispectrum shape information. All we require is the time dependence or growth rate of the bispectrum amplitude. As a first step, the fitting formula (64) can be normalised to the measured bispectrum size by multiplying it with the normalisation factor

$$N_{\text{fit}} \equiv \frac{\|\hat{B}\|}{\|B_{\delta}^{\text{fit}}\|}, \quad (65)$$

Simulation	$L[\frac{\text{Mpc}}{h}]$	$c_{1,2}$	$n_h^{(\text{prim})}$	$\min_{z \leq 20} \mathcal{C}_{\beta,\alpha}$	$\mathcal{C}_{\beta,\alpha}(z=0)$
G512g	1600	4.1×10^6	7	99.8%	99.8%
Loc10	1600	2×10^3	6	99.7%	99.8%
Eq100	1600	8.6×10^2	6	97.9%	99.4%
Flat10	1600	1.2×10^4	6	98.8%	98.9%
Orth100	1600	-3.1×10^2	5.5	91.0%	91.0%
G_{400}^{512}	400	1.0×10^7	8	99.8%	99.8%
Loc10_{400}^{512}	400	$2 \times 10^3 dD/da$	7	98.2%	99.0%
Eq100_{400}^{512}	400	$8.6 \times 10^2 dD/da$	7	94.4%	97.9%
$\text{Flat10}_{400}^{512}$	400	$1.2 \times 10^4 dD/da$	7	97.7%	99.1%
$\text{Orth100}_{400}^{512}$	400	-2.6×10^2	6.5	97.3%	98.9%

Table III. Fitting parameters c_1 and n_h for the fit (63) of the matter bispectrum for Gaussian initial conditions (simulations G512g and G_{400}^{512}) and c_2 and n_h^{prim} for the fit (68) of the primordial bispectrum (57). The two columns on the right show the minimum shape correlation with the measured (excess) bispectrum in N -body simulations, which was measured at redshifts $z = 49, 30, 20, 10, 9, 8, \dots, 0$, and the shape correlation at $z = 0$. For the equilateral case the minimum shape correlation can be improved to 99.4% if the term $4.6 \times 10^{-5} f_{\text{NL}} \bar{D}(z)^{0.5} [2P_{\delta}(k_1)P_{\delta}(k_2)F_2^{(s)}(\mathbf{k}_1, \mathbf{k}_2) + 2 \text{ perms}]$ is added to (68).

which is shown by the dotted line in the lower panels of Fig. 16. While it varies with redshift between 0.7 and 1.4 for $k_{\max} = 2h/\text{Mpc}$, it deviates by at most 8% from unity for $k_{\max} = 0.5h/\text{Mpc}$. The lower panels also show the measured integrated bispectrum size $\|\hat{B}\|$ and the two individual contributions to (63) when the normalisation factor N_{fit} is included. These quantities are divided by $\|B_{\delta,\text{NL}}^{\text{grav}}\|$ for convenience. At high redshifts the total

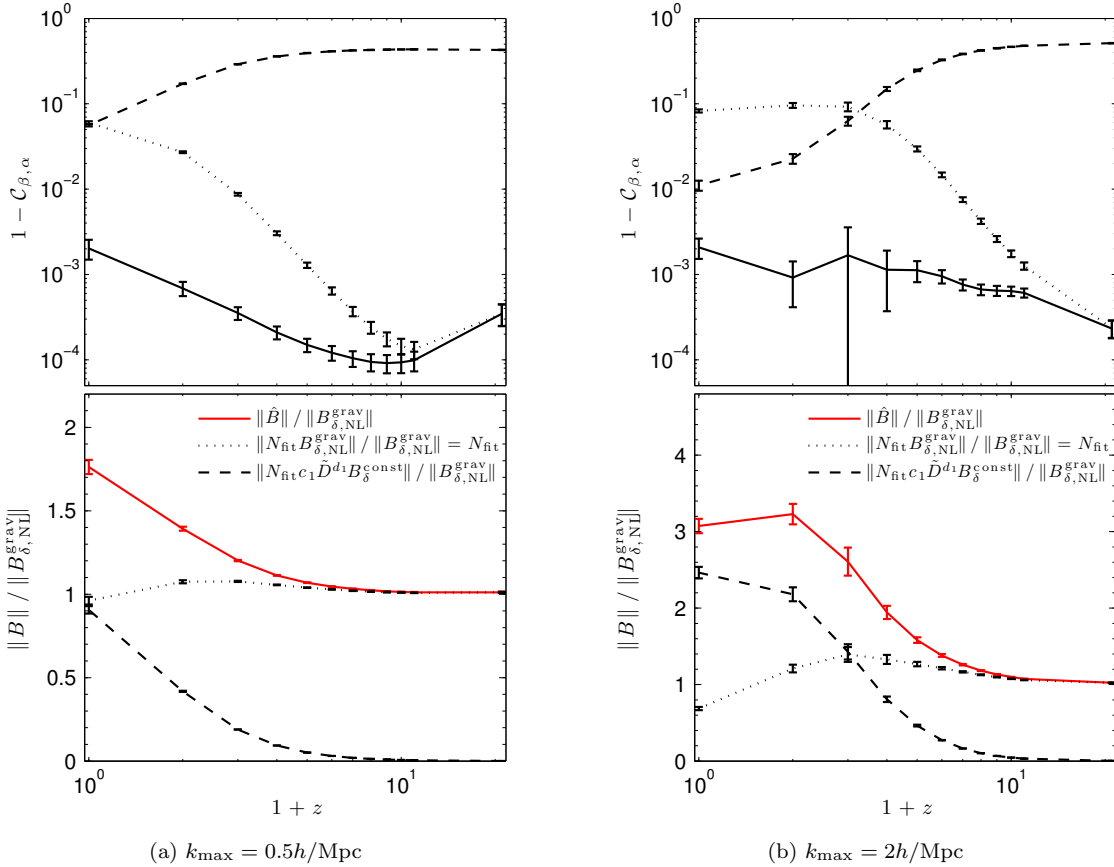


Figure 16. *Upper panels:* Shape correlation of estimated bispectrum in (a) G512g and (b) G₄₀₀⁵¹² simulations with the full fitting formula (63) (solid black), the shape $B_{\delta,\text{NL}}^{\text{grav}}$ as defined in (8) (dotted black) and the shape $B_{\delta,\text{const}}^{\text{grav}}$ as defined in (14) (dashed black). All correlations were calculated with 120 modes Q_n for (a) $k \in [0.004, 0.5]h/\text{Mpc}$ and (b) $k \in [0.016, 2]h/\text{Mpc}$. *Lower panels:* Integrated size of the measured bispectrum (red) and the contributions $N_{\text{fit}}B_{\delta,\text{NL}}^{\text{grav}}$ (dotted black) and $N_{\text{fit}}B_{\delta,\text{const}}^{\text{grav}}$ (dashed black). All these bispectrum sizes are divided by the size of $B_{\delta,\text{NL}}^{\text{grav}}$ for convenience. The normalisation factor N_{fit} is defined in (65) and equals the dotted black curve.

bispectrum size is essentially given by the contribution from $B_{\delta,\text{NL}}^{\text{grav}}$, which equals the tree level prediction for the gravitational bispectrum in this regime. The contribution from $B_{\delta}^{\text{const}}$ dominates at $z \leq 2$ for $k_{\text{max}} = 2h/\text{Mpc}$ when filamentary and spherical nonlinear structures are apparent. A similar transition can be seen at later times on larger scales in Fig. 16a, indicating self-similar behaviour.

It is worth noting that the high integrated correlation between the simple fit (63) and measurements does not imply that all triangle configurations agree perfectly and sub-percent level differences between shape correlations can in principle contain important information, e.g. about the observationally relevant squeezed limit which only makes a small contribution to the total tetrapyd integral over the signal-to-noise weighted dark matter bispectrum. However, if we observed the dark matter bispectrum directly, these shapes would be hard to distinguish because the shape correlation contains the signal-to-noise weighting. Modified shape cor-

relation weights and additional basis functions have been used for better quantitative comparison of the squeezed limit of dark matter bispectra, but this is left for a future publication.

Alternative phenomenological fit

An alternative fitting formula with 9 fitting parameters and calibrated on larger scales was given in [14] and summarised in this paper in Section III. In the range of validity given by [14], $0.03h/\text{Mpc} \leq k \leq 0.4h/\text{Mpc}$ at $0 \leq z \leq 1.5$, we find good agreement with our N -body measurements, see green circles in Fig. 14d and Fig. 14e. Without having to run N -body simulations with higher resolutions, we extended the bispectrum measurement to $k_{\text{max}} = 0.86h/\text{Mpc}$ with the fast separable estimator, see red symbols in Fig. 14d and Fig. 14e. In this extended regime the fitting formula of [14] still has a shape correlation of 99.5% or more with the measured bispectrum

at $z \leq 1.5$, but underestimates the cumulative signal to noise by up to 11%. Our measured β_n^R coefficients or our simple fit (63) can be used as alternative fitting formulae for the gravitational bispectrum valid to smaller scales, $k_{\max} \leq 2h/\text{Mpc}$, and for all redshifts $z \leq 20$.

Halo model

The halo model prediction for the Gaussian dark matter bispectrum yields a remarkably high shape correlation of more than 99.7% with the measured bispectrum at $z = 0$ for $k_{\max} = 2h/\text{Mpc}$. While the halo model bispectrum has been tested on some one-dimensional slices in [37] and on larger scales in [38], the result presented here demonstrates that at $z = 0$ the halo model shape is a good representation of the shape measured in N -body simulations over the full tetrapyd allowed by the triangle condition. At higher redshifts, when less dark matter resides in halos, the halo model prediction becomes worse and alternative phenomenological approaches like the ones discussed above yield higher shape correlations with the measured bispectrum. A more thorough examination of the halo model will be presented in [35].

VII. PRIMORDIAL NON-GAUSSIAN BISPECTRUM RESULTS

Primordial bispectrum measurements

We have set up and evolved non-Gaussian initial conditions for local models with $f_{\text{NL}}^{\text{loc}} = -10, 10, 20, 50$ using (30), for equilateral models with $f_{\text{NL}}^{\text{eq}} = \pm 100$, for orthogonal models with $f_{\text{NL}}^{\text{orth}} = \pm 100$ and for the flattened model with $f_{\text{NL}}^{\text{flat}} = 10$ using separable expansions as in [26, 27]. Detailed parameters for the N -body simulations are given in Table I.

Local shape

In Fig. 12b we show comparisons of the measured $\beta_n^R - (\beta_n^R)_{\text{Gauss}}$ coefficients with the expansion coefficients α_n^R of the linearly evolved primordial bispectrum (24) for $f_{\text{NL}}^{\text{loc}} = 10$, finding good agreement at early times, but deviations at late times which are scale-dependent. The most obvious feature as we consider increasingly nonlinear wavenumbers is the emergence of a large constant or equilateral signal. Indeed Fig. 13 shows this signal on small scales with the late time bispectrum also exhibiting an enhanced signal in the squeezed limit.

In Fig. 17a we plot the projection $f_{\text{NL}}^{\text{loc}}$ of the measured non-Gaussian bispectrum \hat{B}_{NG} on the linearly evolved primordial bispectrum (see (24) and (31)), their shape correlation $\mathcal{C}_{\beta,\alpha}$, cumulative signal to noise $\|\hat{B}_{\text{NG}}\|$

and total integrated bispectrum normalised to the local shape, $\bar{F}_{\text{NL}}^{\hat{B}_{\text{NG}}}$. We also show the shape correlation $\mathcal{C}_{\text{NG,G}}$ between \hat{B}_{NG} and the bispectrum measured in Gaussian simulations. For $z = 0$ and $k \in [0.0039, 0.5] h/\text{Mpc}$ the linearly evolved primordial bispectrum underpredicts the measured cumulative signal to noise $\|\hat{B}_{\text{NG}}\|$ by a factor of 8 and has a shape correlation with the measured bispectrum of about 0.6, implying that the projection $f_{\text{NL}}^{\text{loc}}$ is about 4.8 times the input value of $f_{\text{NL}}^{\text{loc}} = 10$. The green and blue symbols in Fig. 17a show that tree level perturbation theory improves if we consider larger scales, as expected.

Other shapes

We also run simulations with equilateral, orthogonal and flattened non-Gaussian initial conditions using the separable expansion method [26, 27]. Bispectrum measurements are shown in Figures 3, 13, 17 and 18. As in the local case we find agreement with tree level perturbation theory at all times on large scales. However on small scales and at late times, Fig. 13 shows that the measured bispectrum for equilateral initial conditions has additional equilateral and flattened contributions compared to the linearly evolved input bispectrum (24). For initial conditions with the $f_{\text{NL}}^{\text{orth}} = 100$ orthogonal shape, which is positive for equilateral configurations and negative for flattened and squeezed configurations, we find that the late time small scale bispectrum turns slightly negative for equilateral configurations and is more negative in flattened and squeezed configurations than the linearly evolved input bispectrum. The bispectrum from flattened initial conditions shows additional contributions compared to the tree level prediction. For orthogonal and flattened initial conditions the late time bispectra have a large signal in the squeezed limit, leading to possible confusion with local shape initial conditions (with negative $f_{\text{NL}}^{\text{loc}}$ for positive input $f_{\text{NL}}^{\text{orth}}$ and positive $f_{\text{NL}}^{\text{loc}}$ for positive input $f_{\text{NL}}^{\text{flat}}$). However scale dependent halo bias is sensitive to the scaling in the squeezed limit and can therefore help to disentangle such shapes (see e.g. [10, 24]).

It is worth noting that the shape correlation $\mathcal{C}_{\beta,\alpha}$ between measured and input bispectra drops as we reduce k_{\max} already at the initial time of the simulations, e.g. $\mathcal{C}_{\beta,\alpha} \approx 0.95$ for $k_{\max} = 0.13h/\text{Mpc}$ in the equilateral case. This indicates that the initial conditions generated with a separable mode expansion - which are generated at $k_{\max} = 0.5h/\text{Mpc}$ - are not a perfect fit to the shape when restricted to large scales. This is to be expected since the expansion is optimised to fit the total cumulative signal to noise up to $k_{\max} = 0.5h/\text{Mpc}$. There are however several possibilities of further improving the

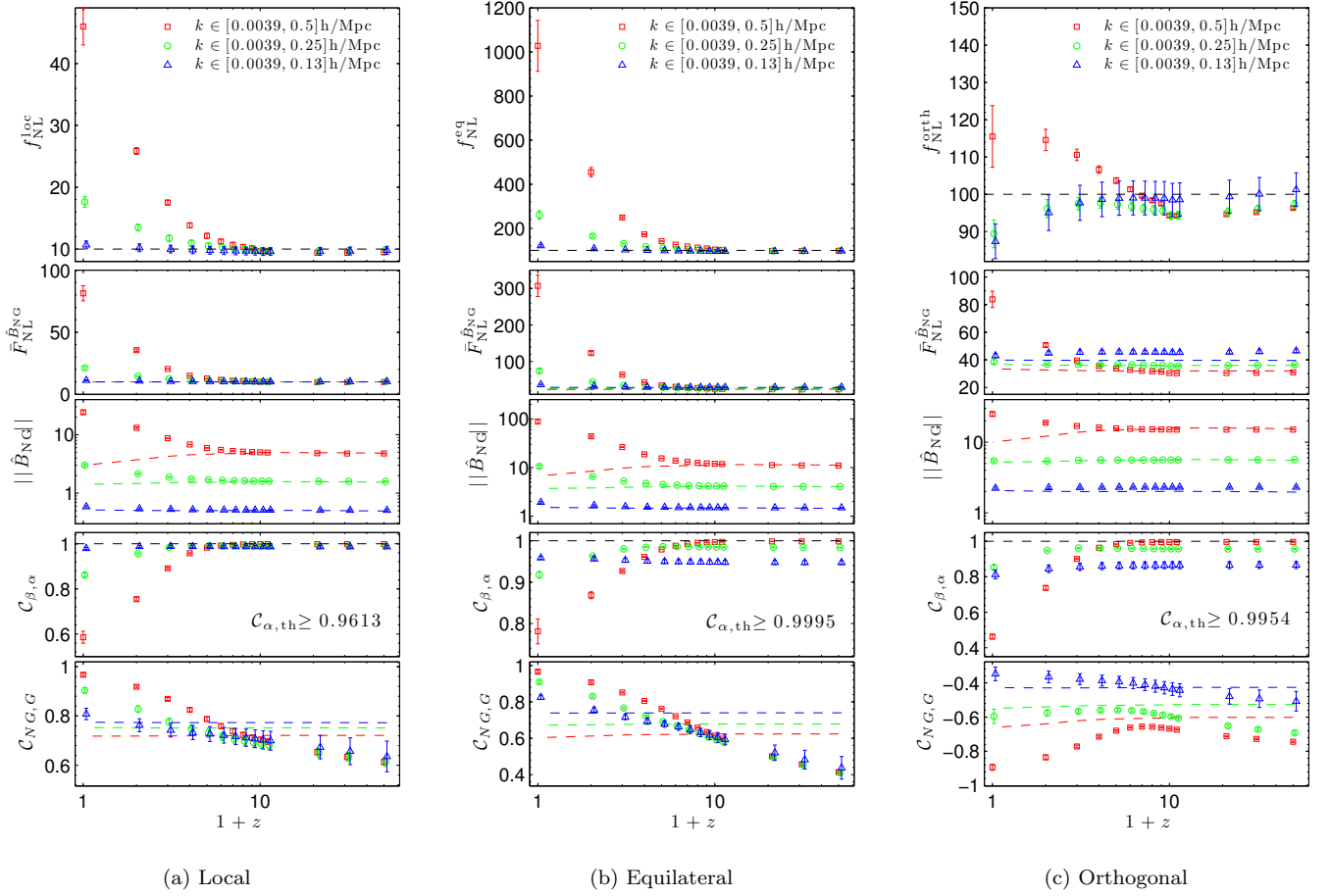


Figure 17. Dark matter bispectrum quantities as in Fig. 14 but for the non-Gaussian simulations Loc10, Eq100 and Orth100 with local, equilateral and orthogonal initial conditions, respectively. The non-Gaussian bispectrum is computed with (57) and then compared to the tree level prediction (24) (dashed lines). The lowest panel shows the shape correlation of the measured non-Gaussian bispectrum with the measured bispectrum for Gaussian initial conditions.

initial conditions on large scales. One could add basis functions which are localised on large scales or one could introduce optimised separable weighting functions in the mode expansions. This would be particularly important for examining halo bias which is very sensitive to the squeezed limit and therefore to large scale modes. However for studying the global behaviour of the dark matter bispectrum we find it acceptable that the shape of the initial conditions is not perfect on very large scales and leave further improvements of the initial conditions for future work.

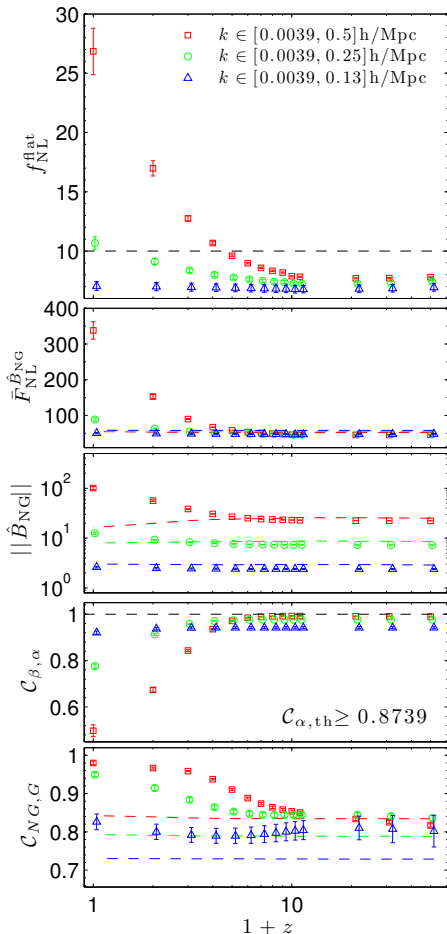


Figure 18. Like Fig. 17 but for simulation Flat10 with flattened non-Gaussian initial conditions.

Loop corrections for primordial non-Gaussianity

As is apparent from Figures 13, 17 and 18, the tree level prediction for the non-Gaussian matter bispectrum breaks down for small scales and low redshift. The inclusion of loop corrections described in [11] is expected to improve the fit at such scales and redshifts. First results

on the correlation between the observations and theoretical prediction $C_{\beta,\alpha}$ indicate that 1-loop corrections can vastly improve the shape correlation in the nonlinear regime to $\mathcal{O}(0.8 - 0.9)$, while shape correlations of more than 0.9 at $k = 0.5h/\text{Mpc}$ and $z = 0$ may require higher order loop corrections. However we defer a detailed analysis of loop corrections and more phenomenological halo model approaches to a forthcoming paper.

Linearity in input f_{NL}

We test if $\mathcal{O}(f_{\text{NL}}^2)$ corrections are important by comparing simulations with $f_{\text{NL}}^{\text{loc}} = -10, 20$ and 50 to the $f_{\text{NL}}^{\text{loc}} = 10$ simulation in Fig. 19a (with box size $L = 1600\text{Mpc}/h$). The curves in all three panels would be exactly unity in case of perfect linearity in the input f_{NL} . Deviations from linearity are at most 1%.

In case of equilateral and orthogonal initial conditions we compare simulations with input $f_{\text{NL}} = \pm 100$. The equilateral shape gives similar results to the local shape, see Fig. 19b. For the orthogonal shape the shape correlation between theory and measurements deviates from linearity in the input f_{NL} by about 3% at $z = 0$ for $k_{\text{max}} = 0.5h/\text{Mpc}$ and the total integrated bispectrum differs by less than 5%. These two effects cancel each other approximately so that the measured projection $f_{\text{NL}}^{\text{orth}}$ only deviates by less than 1.5% from linearity.

We conclude that at the $\mathcal{O}(5\%)$ level the bispectra measured in our large scale simulations can be scaled to other values $f_{\text{NL}}^{\text{new}}$ fulfilling $|f_{\text{NL}}^{\text{loc}}| \leq 50$, $|f_{\text{NL}}^{\text{Eq}}| \leq 100$ and $|f_{\text{NL}}^{\text{Orth}}| \leq 100$ using the linear scaling

$$B_{\text{NG}}(f_{\text{NL}}^{\text{new}}) = \frac{f_{\text{NL}}^{\text{new}}}{f_{\text{NL}}} \hat{B}_{\text{NG}}(f_{\text{NL}}). \quad (66)$$

Fitting formulae for non-Gaussian simulations

Separable polynomial fits

Matter bispectra for non-Gaussian initial conditions of the local, equilateral, orthogonal and flattened type are described by the β_n^R coefficients in Table II. These polynomial fitting formulae can serve as a starting point for future work that relies on non-Gaussian dark matter bispectra in the nonlinear regime.

Time-shift model fits

Simple fitting formulae for the primordial contribution to the matter bispectrum can be successfully obtained from the halo time-shift model described in section III. Before discussing this fit in detail, we perform a simple

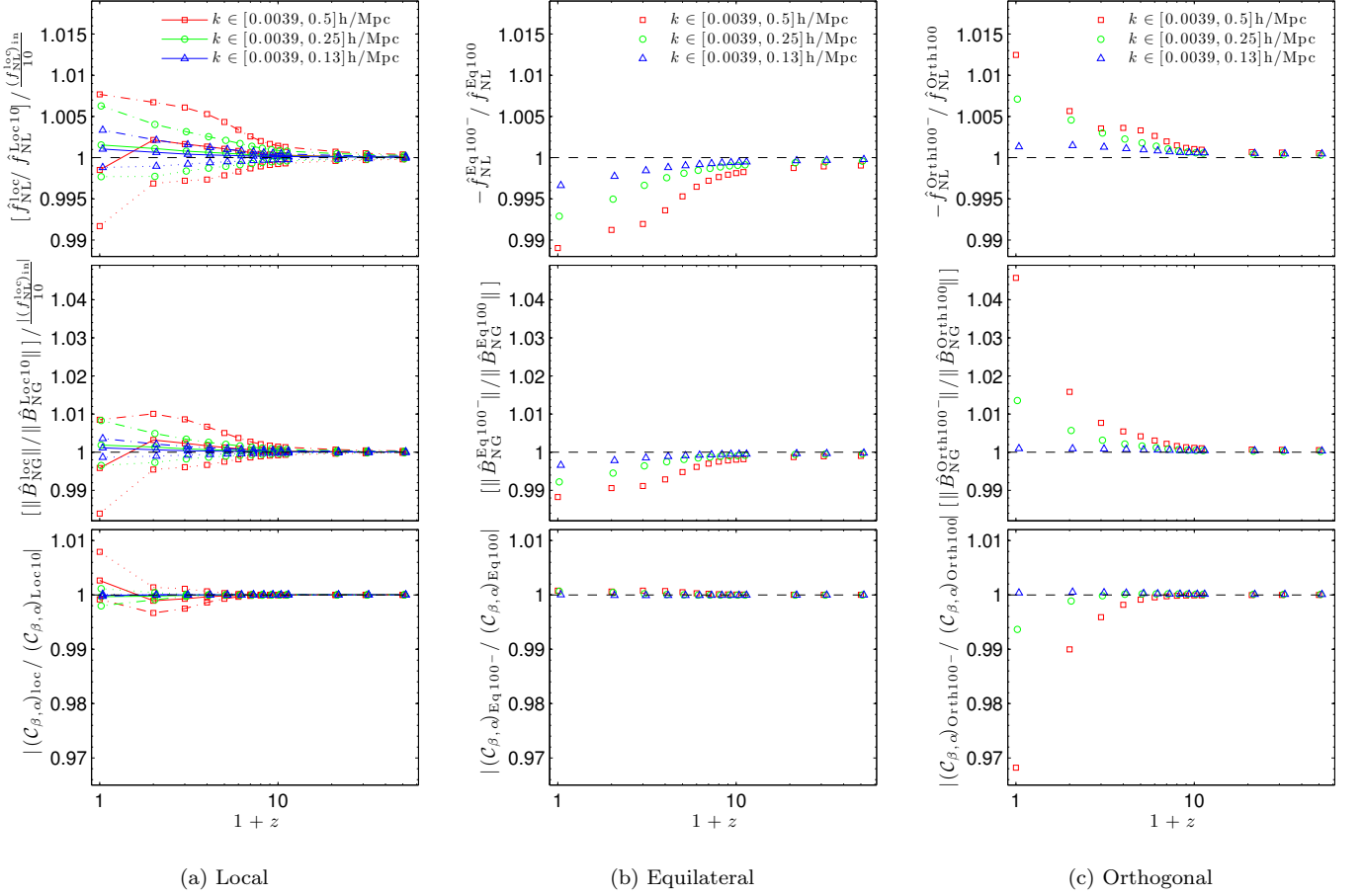


Figure 19. Test if the bispectrum contributions (57) from non-Gaussian initial conditions are linear in the input f_{NL} . (a) Ratios of Loc20 (solid line), Loc50 (dash-dot line) and Loc10⁻ (dotted line) to Loc10. The label 'loc' stands for Loc20, Loc50 and Loc10⁻. We scale the curves by $(f_{\text{NL}}^{\text{loc}})_{\text{in}}/10$ so that in case of perfect linearity in f_{NL} all curves were unity. (b) Ratio of Eq100⁻ to Eq100 simulation. (c) Ratio of Orth⁻ to Orth100 simulation.

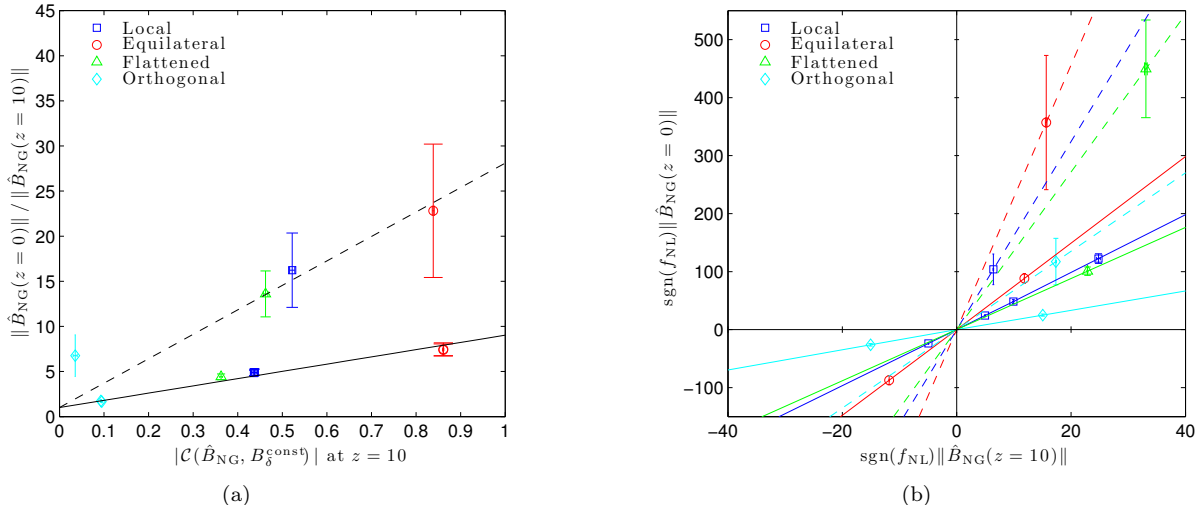


Figure 20. (a) Relative growth of bispectrum size between $z = 10$ and $z = 0$ as a function of the absolute value of the shape correlation between the measured non-Gaussian bispectrum \hat{B}_{NG} and the shape $B_{\delta}^{\text{const}}$ defined in (14) at redshift $z = 10$, testing relation (67). The plot contains all simulations shown in (b) but data points which only differ in the input f_{NL} are almost indistinguishable. Regression lines through (0, 1) are shown for $k_{\text{max}} = 0.5h/\text{Mpc}$ (continuous) and $k_{\text{max}} = 2h/\text{Mpc}$ (dashed). (b) Bispectrum size at redshift $z = 0$ as a function of the bispectrum size at high redshift, $z = 10$, for different primordial shapes (see legend). Continuous lines correspond to $k_{\text{max}} = 0.5h/\text{Mpc}$ while dashed lines correspond to $k_{\text{max}} = 2h/\text{Mpc}$ simulations. Different points on one line show results for different input f_{NL} .

consistency check of the basic idea of the model. The relatively fast growth of the constant bispectrum implies that it constitutes the dominant contribution to the non-Gaussian bispectrum B_{NG} at sufficiently small scales and late time z_{late} . The amplitude of this constant bispectrum is related to the projection of the non-Gaussian bispectrum B_{NG} on the constant shape at the time z_{early} when halos start to form (and thereafter). Hence we expect that

$$\|B_{\text{NG}}(z_{\text{late}})\| \propto \mathcal{C}(B_{\text{NG}}(z_{\text{early}}), B_{\delta, \text{const}}^{\text{grav}}(z_{\text{early}})) \times \|B_{\text{NG}}(z_{\text{early}})\|. \quad (67)$$

This simple expectation is approximately seen in Fig. 20a for the local, equilateral and flattened shapes, confirming the basic idea of the time-shift model. The fact that the orthogonal shape deviates somewhat could be related to the change of sign of the orthogonal shape for different triangle configurations. Note that relation (67) and Fig. 20a are interesting results on their own because they show that the relative growth of the non-Gaussian bispectrum can be predicted from its correlation with the constant shape at early times. Fig. 20b illustrates the absolute values of the measured bispectrum sizes which were used to produce Fig. 20a.

In detail, the simple fitting formulae for the non-Gaussian bispectra are obtained by combining the partially loop-corrected tree level expression (25) with the

constant shape (28) as

$$B_{\text{NG}}^{\text{fit}}(k_1, k_2, k_3) \equiv f_{\text{NL}} [B_{\delta, \text{NL}}^{\text{prim}} + B_{\delta, \text{const}}^{\text{prim}}]. \quad (68)$$

The fitting parameters c_2 and n_h^{prim} in (28) are listed in Table III. Similar to the Gaussian case they were obtained by analytically determining the optimal weight $w(z)$ for the ‘constant’ $(k_1 + k_2 + k_3)^\nu$ contribution and approximating this with $c_2 \bar{D}(z)^{n_h^{\text{prim}}}$ (see green and black dashed lines in Fig. 21). As expected from Section III we find $n_h^{\text{prim}} = n_h - 1$ for local, equilateral and flattened initial conditions.

Table III also shows the shape correlation with the measured excess bispectrum (57). These shape correlations are remarkably good given the simplicity of (68), especially for local, equilateral and flattened initial conditions. The impact of the orthogonal shape on the matter bispectrum seems to be somewhat harder to model, which is reflected in the fact that our simple model performs worse for this shape. This is expected because the orthogonal shape contains almost no constant component, the dominant evolution of which is the basis for the simple time-shift model. While the integrated bispectrum size \bar{F}_{NL} of the fitting formulae is consistent with the measured bispectrum size at high redshift and at $z = 0$, it underestimates the measured size at the 10 – 20% level at intermediate redshifts for $k_{\text{max}} = 0.5h/\text{Mpc}$. This could be improved by adding more shapes or by using a redshift-dependent normalisation factor in (68) similar to the N_{fit} factor in the Gaus-

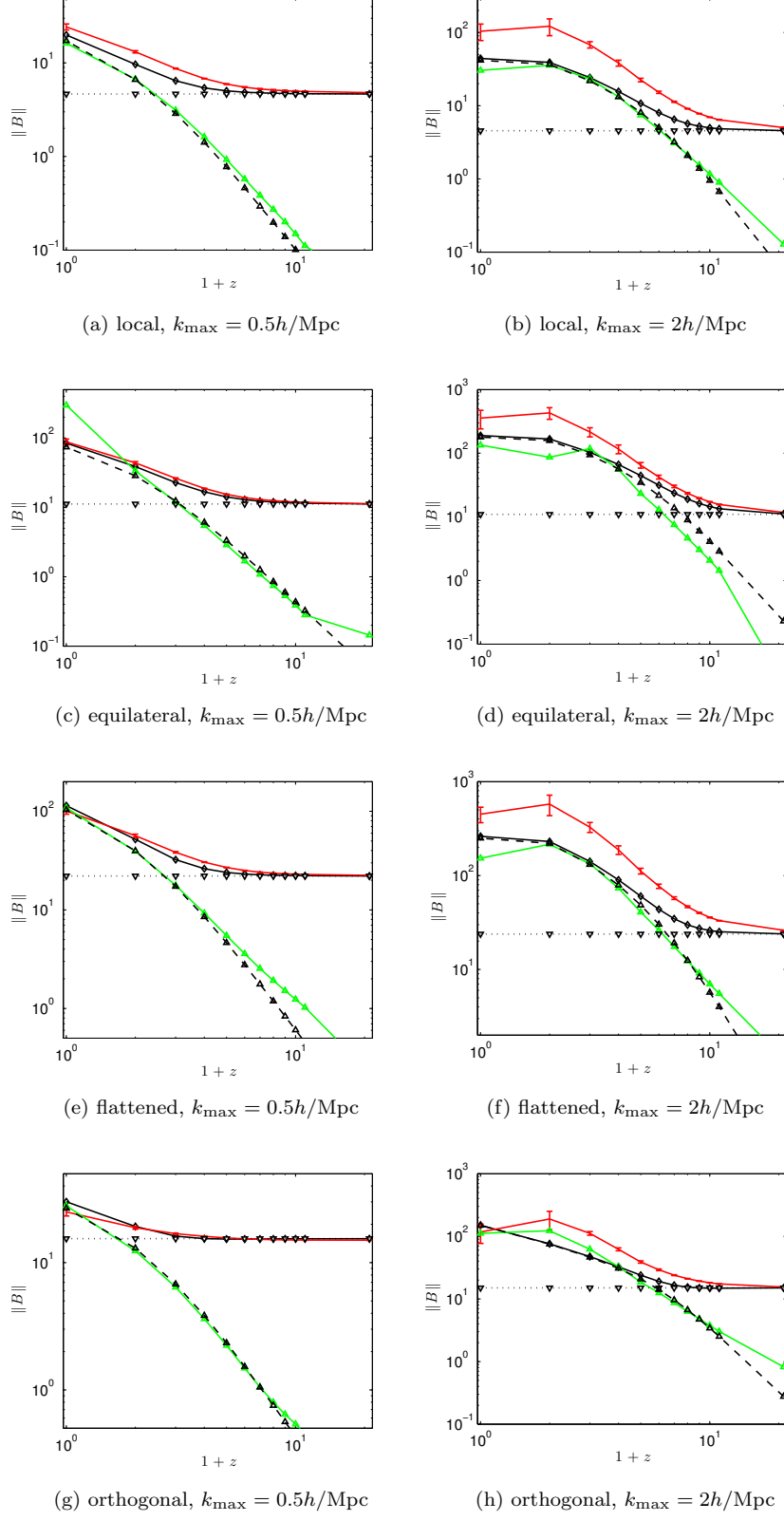


Figure 21. Contributions to simple non-Gaussian fits (68). The arbitrary weight $w(z)$ in $B_{\text{NG}}^{\text{opt}} = B_{\delta, \text{NL}}^{\text{prim}} + w(z)(k_1 + k_2 + k_3)^\nu$ is determined analytically such that $\mathcal{C}(\hat{B}_{\text{NG}}, B_{\text{NG}}^{\text{opt}})$ is maximal (for $\nu = -1.7$). We plot $\|B_{\delta, \text{NL}}^{\text{prim}}\|$ (black dotted), $\|w(z)(k_1 + k_2 + k_3)^\nu\|$ (green) and $B_{\delta, \text{const}}^{\text{prim}}$ (black dashed) as defined in (28) with fitting parameters given in Table III. The continuous black and red curves show $\|B_{\text{NG}}^{\text{fit}}\|$ from (68) and the estimated primordial bispectrum size $\|\hat{B}_{\text{NG}}\|$, respectively.

sian case. On smaller scales, $k_{\max} = 2h/\text{Mpc}$, the non-Gaussian fitting formulae provide a less accurate overall fit, but we also list them in Table III for completeness and because the correlations at $z = 0$ are quite high.

It should be noted that simple fits like the ones presented here may be somewhat more important in the mildly nonlinear regime than in the strongly nonlinear regime because the halo model (extended to non-Gaussian initial conditions) should be able to describe the strongly nonlinear regime. We leave more accurate extensions of the simple fits for non-Gaussian initial conditions and more quantitative comparisons with loop corrections and halo model predictions for future work [35].

Redshift at which 1-halo contribution becomes important

We determine the redshift z_* at which the approximate 1-halo bispectrum $B_{\delta}^{\text{const}}$ in the simple fits of the bispectrum for non-Gaussian initial conditions becomes important by matching

$$\|C(B_{\delta,\text{NL}}^{\text{prim}}(z_*), B_{\delta,\text{const}}^{\text{prim}}(z_*))B_{\delta,\text{NL}}^{\text{prim}}(z_*)\| = \|B_{\delta,\text{const}}^{\text{prim}}(z_*)\|. \quad (69)$$

For $k_{\max} = 0.5h/\text{Mpc}$ we find $z_* = 3.5, 3.3, 4.3$ for local, equilateral and flattened initial conditions, respectively. For $k_{\max} = 2h/\text{Mpc}$ we find instead $z_* = 8.5, 8$ and 9.6 for the same initial conditions. The orthogonal shape has almost no constant part. We therefore get somewhat different values of $z_* = 5.5$ and 11 for $k_{\max} = 0.5h/\text{Mpc}$ and $k_{\max} = 2h/\text{Mpc}$, respectively. This demonstrates that the time at which nonlinear structures contribute significantly to the perturbative prediction for the primordial bispectrum is earlier on smaller scales.

VIII. SUMMARY AND CONCLUSIONS

We have presented an implementation of a bispectrum estimator for N -body simulations using a separable modal expansion of the bispectrum as described in [26]. While a brute force estimation of the full bispectrum is computationally expensive, requiring $\mathcal{O}(N^6)$ operations for N particles per dimension, we find that the gravitational and the most prominent primordial bispectra can be approximated by only $n_{\max} = \mathcal{O}(50)$ separable basis functions (for the range of scales relevant for N -body simulations). The bispectrum projection on the corresponding subspace of all possible bispectra is estimated with $\mathcal{O}(n_{\max}N^3)$ operations, which is faster than brute force estimation by a factor of $\mathcal{O}(N^3/n_{\max}) \sim \mathcal{O}(10^7)$ for typical simulations. Thus the computational cost for accurate 3D bispectrum estimation is almost negligible compared to the cost for running the N -body simulations (e.g. we can estimate the full bispectrum of a

1024^3 grid up to $k_{\max} = \frac{N}{4} \frac{2\pi}{L}$ in one hour on only 6 cores). This allows us to estimate the bispectrum as a standard simulation diagnostic whenever the power spectrum is measured. Expressing the bispectrum using its n_{\max} separable components yields a radical compression of data which simplifies further analysis like comparisons between theory and simulations. The separable bispectrum estimator therefore provides a very useful additional statistic characterising the formation of structures in N -body simulations, with high sensitivity to different shapes of primordial non-Gaussianity corresponding to different models of inflation.

We have performed many N -body simulations with Gaussian initial conditions as well as non-Gaussian initial conditions of the local, equilateral, orthogonal and (non-separable) flattened shape, exploiting the separable bispectrum expansion for efficient generation of initial conditions as described for primordial fields in [26, 27]. On large scales the measured gravitational and primordial bispectra agree with leading order perturbation theory and with measurements for Gaussian initial conditions by [14] in the mildly nonlinear regime, demonstrating the unbiasedness of the estimator and the initial conditions. In the nonlinear regime, the gravitational bispectrum becomes dominated by a large ‘constant’ signal receiving elongated and equilateral contributions not captured by tree level perturbation theory. However, it remains suppressed in the squeezed limit, where primordial bispectrum signals can peak (see Fig. 13).

Our measured N -body bispectra for Gaussian and non-Gaussian simulations can be expressed by 50 components β_n^R , which we provide in Table II for the key models. They can be used as fitting formulae for the gravitational and primordial bispectrum in the nonlinear regime.

Less accurate but simpler fitting formulae are obtained by modeling the bispectrum as a combination of partially loop-corrected perturbative bispectra and a simple ‘constant’ bispectrum, which is constant on slices $\sum k_i = \text{const.}$ and which is obtained as an approximation to the 1-halo bispectrum. While the former contribution dominates on large scales and early times, the latter constant contribution dominates in the nonlinear regime. Interpreting the effect of primordial non-Gaussianity on the constant bispectrum contribution as a time-shift with respect to Gaussian simulations allows us to model the time dependence of the constant bispectrum contribution for non-Gaussian initial conditions. For Gaussian initial conditions, the simple fits achieve a shape correlation of at least 99.8% with the measured gravitational bispectrum for $z \leq 20$ and $k_{\max} = \{0.5, 2\}h/\text{Mpc}$. For local, equilateral and flattened non-Gaussian initial conditions the primordial bispectrum is fitted with a shape correlation of at least 97.9% at $z = 0$ and at least 94.4% for $z \leq 20$ (with correlation typically $\gtrsim 98\%$ for most shapes and redshifts, see Table III). The impact of the orthogonal shape seems to be somewhat harder to model,

because it does not have a constant component initially, but our simple fit still achieves correlations of at least 91% for $z \leq 20$.

Throughout this work we have visualised the measured bispectra in three-dimensional tetrapyd plots [8], which show the bispectrum shape and amplitude at different length scales and generalise commonly used plots of one- or two-dimensional slices through the tetrapyd volume. For a more quantitative analysis, particularly to test analytic predictions and fitting formulae, we have made extensive use of full three-dimensional shape correlations, the cumulative signal-to-noise of the bispectra and their projection f_{NL} on theoretical shapes. These quantities have been evaluated extremely efficiently using the bispectrum components obtained from the separable estimator.

We find that regular grid initial conditions produce an initial spurious bispectrum due to the anisotropy of the regular grid, which can be avoided by using glass initial conditions. However the difference between regular grid and glass initial conditions decreases with time as gravitational perturbations grow such that both initial conditions yield similar results at late times. Effects of order f_{NL}^2 were shown to affect the bispectrum measurements by less than 5% in our large scale simulations.

Clearly, further work is required to study the effects of general primordial non-Gaussianity on observable quantities like the bispectrum of galaxies, particularly in the nonlinear regime. However the present work represents, we believe, an important step forward in the understanding of structure formation in the presence of primordial non-Gaussianity and the search for primordial non-Gaussianity in large scale structures.

ACKNOWLEDGEMENTS

We are especially grateful to James Fergusson for his work on the development of the separable bispectrum estimation formalism, for sharing his experience with the application to the CMB and for many informative and illuminating discussions regarding the application to large scale structures. We thank Anthony Challinor for comments on the manuscript and Daniel Baumann, Francis Bernardeau, Anthony Challinor, Hiro Funakoshi, Helge Gruetjen, Martin Haehnelt, Antony Lewis and Emiliano Sefusatti for very helpful discussions. We are also very grateful to Andrey Kaliazin for his invaluable computational help. We thank Volker Springel for providing us the Gadget-3 N -body code (see [62, 63] for older versions). We also thank Edwin Sirko for his initial conditions code [67], parts of which we use for setting up initial conditions, Sebastian Pueblas and Roman Scoccimarro for their public 2LPT code for Gaussian initial conditions [61] and Antony Lewis and Anthony Challinor for CAMB [28]. We acknowledge the use of the FFTW3

library and SPLASH [68] for visualising particle distributions. Simulations were performed on the COSMOS supercomputer (an Altix 4700) which is funded by STFC, HEFCE and SGI. MMS was supported by the Science and Technology Facilities Council, DAMTP Cambridge and St John's College Cambridge. DMR was supported by the Science and Technology Facilities Council grant ST/I000976/1. EPSS was supported by the STFC grant ST/F002998/1 and the Centre for Theoretical Cosmology.

-
- [1] E. Komatsu, K. M. Smith, J. Dunkley, C. L. Bennett, B. Gold, G. Hinshaw, N. Jarosik, D. Larson, M. R.olta, L. Page, et al., *ApJS* **192**, 18 (2011), 1001.4538.
 - [2] J. R. Fergusson, M. Liguori, and E. P. S. Shellard, *ArXiv e-prints* (2010), 1006.1642.
 - [3] J. Smidt, A. Amblard, C. T. Byrnes, A. Cooray, A. Heavens, and D. Munshi, *Phys. Rev. D* **81**, 123007 (2010), 1004.1409.
 - [4] J. R. Fergusson, D. M. Regan, and E. P. S. Shellard, *ArXiv e-prints* (2010), 1012.6039.
 - [5] A. Slosar, C. Hirata, U. Seljak, S. Ho, and N. Padmanabhan, *JCAP* **8**, 31 (2008), 0805.3580.
 - [6] J.-Q. Xia, C. Baccigalupi, S. Matarrese, L. Verde, and M. Viel, *JCAP* **8**, 33 (2011), 1104.5015.
 - [7] J. R. Fergusson and E. P. S. Shellard, *Phys. Rev. D* **80**, 043510 (2009), 0812.3413.
 - [8] J. R. Fergusson, M. Liguori, and E. P. S. Shellard, *Phys. Rev. D* **82**, 023502 (2010), 0912.5516.
 - [9] D. M. Regan, E. P. S. Shellard, and J. R. Fergusson, *Phys. Rev. D* **82**, 023520 (2010), 1004.2915.
 - [10] N. Dalal, O. Doré, D. Huterer, and A. Shirokov, *Phys. Rev. D* **77**, 123514 (2008), 0710.4560.
 - [11] E. Sefusatti, *Phys. Rev. D* **80**, 123002 (2009), 0905.0717.
 - [12] E. Sefusatti, M. Crocce, and V. Desjacques, *MNRAS* **406**, 1014 (2010), 1003.0007.
 - [13] R. Scoccimarro and H. M. P. Couchman, *MNRAS* **325**, 1312 (2001), arXiv:astro-ph/0009427.
 - [14] H. Gil-Marín, C. Wagner, F. Fragkoudi, R. Jimenez, and L. Verde, *JCAP* **2**, 47 (2012), 1111.4477.
 - [15] K. Chuen Chan, R. Scoccimarro, and R. K. Sheth, *ArXiv e-prints* (2012), 1201.3614.
 - [16] N. Hamaus, U. Seljak, and V. Desjacques, *Phys. Rev. D* **84**, 083509 (2011), 1104.2321.
 - [17] E. Sefusatti, M. Crocce, and V. Desjacques, *ArXiv e-prints* (2011), 1111.6966.
 - [18] M. Manera, R. K. Sheth, and R. Scoccimarro, *MNRAS* **402**, 589 (2010), 0906.1314.
 - [19] V. Desjacques, D. Jeong, and F. Schmidt, *Phys. Rev. D* **84**, 063512 (2011), 1105.3628.
 - [20] K. M. Smith and M. LoVerde, *JCAP* **11**, 9 (2011), 1010.0055.
 - [21] V. Desjacques and U. Seljak, *Classical and Quantum Gravity* **27**, 124011 (2010), 1003.5020.
 - [22] J.-Q. Xia, A. Bonaldi, C. Baccigalupi, G. De Zotti, S. Matarrese, L. Verde, and M. Viel, *JCAP* **8**, 13 (2010), 1007.1969.
 - [23] C. Wagner, L. Verde, and L. Boubekur, *JCAP* **10**, 22 (2010), 1006.5793.

- [24] C. Wagner and L. Verde, *JCAP* **3**, 2 (2012), 1102.3229.
- [25] R. Scoccimarro, L. Hui, M. Manera, and K. C. Chan, *Phys. Rev. D* **85**, 083002 (2012), 1108.5512.
- [26] J. R. Fergusson, D. M. Regan, and E. P. S. Shellard, *ArXiv e-prints* (2010), 1008.1730.
- [27] D. M. Regan, M. M. Schmittfull, E. P. S. Shellard, and J. R. Fergusson, *ArXiv e-prints* (2011), 1108.3813.
- [28] A. Lewis, A. Challinor, and A. Lasenby, *Astrophys. J.* **538**, 473 (2000), arXiv:astro-ph/9911177.
- [29] K. M. Smith, S. Ferraro, and M. LoVerde, *JCAP* **3**, 32 (2012), 1106.0503.
- [30] R. E. Smith, J. A. Peacock, A. Jenkins, S. D. M. White, C. S. Frenk, F. R. Pearce, P. A. Thomas, G. Efstathiou, and H. M. P. Couchman, *MNRAS* **341**, 1311 (2003), arXiv:astro-ph/0207664.
- [31] F. Bernardeau, S. Colombi, E. Gaztanaga, and R. Scoccimarro, *Phys. Rept.* **367**, 1 (2002), astro-ph/0112551.
- [32] R. Scoccimarro, *Astrophys. J.* **487**, 1 (1997), arXiv:astro-ph/9612207.
- [33] J. N. Fry, *Astrophys. J.* **279**, 499 (1984), URL <http://dx.doi.org/10.1086/161913>.
- [34] D. Jeong and E. Komatsu, *Astrophys. J.* **703**, 1230 (2009), 0904.0497.
- [35] D. M. Regan, M. M. Schmittfull, and E. P. S. Shellard (In preparation).
- [36] A. Cooray and R. Sheth, *Phys. Rept.* **372**, 1 (2002), arXiv:astro-ph/0206508.
- [37] P. Valageas and T. Nishimichi, *Astronomy and Astrophysics* **532**, A4 (2011), 1102.0641.
- [38] D. G. Figueroa, E. Sefusatti, A. Riotto, and F. Vernizzi, *ArXiv e-prints* (2012), 1205.2015.
- [39] J. F. Navarro, C. S. Frenk, and S. D. M. White, *Astrophys. J.* **462**, 563 (1996), arXiv:astro-ph/9508025.
- [40] X. Chen, *Advances in Astronomy* **2010**, 638979 (2010), 1002.1416.
- [41] M. Liguori, E. Sefusatti, J. R. Fergusson, and E. P. S. Shellard, *Advances in Astronomy* **2010**, 980523 (2010), 1001.4707.
- [42] N. Bartolo, E. Komatsu, S. Matarrese, and A. Riotto, *Phys. Rept.* **402**, 103 (2004), arXiv:astro-ph/0406398.
- [43] E. Komatsu, *Classical and Quantum Gravity* **27**, 124010 (2010), 1003.6097.
- [44] A. P. S. Yadav and B. D. Wandelt, *Advances in Astronomy* **2010**, 565248 (2010), 1006.0275.
- [45] D. S. Salopek and J. R. Bond, *Phys. Rev. D* **42**, 3936 (1990).
- [46] J. Maldacena, *JHEP* **5**, 13 (2003), arXiv:astro-ph/0210603.
- [47] P. Creminelli and M. Zaldarriaga, *JCAP* **10**, 6 (2004), arXiv:astro-ph/0407059.
- [48] C. Cheung, A. L. Fitzpatrick, J. Kaplan, and L. Senatore, *JCAP* **2**, 21 (2008), 0709.0295.
- [49] M. Alishahiha, E. Silverstein, and D. Tong, *Phys. Rev. D* **70**, 123505 (2004), arXiv:hep-th/0404084.
- [50] D. Baumann and D. Green, *JCAP* **9**, 14 (2011), 1102.5343.
- [51] P. Creminelli, A. Nicolis, L. Senatore, M. Tegmark, and M. Zaldarriaga, *JCAP* **5**, 4 (2006), arXiv:astro-ph/0509029.
- [52] A. Lewis, *JCAP* **10**, 26 (2011), 1107.5431.
- [53] L. Senatore, K. M. Smith, and M. Zaldarriaga, *JCAP* **1**, 28 (2010), 0905.3746.
- [54] X. Chen, M.-x. Huang, S. Kachru, and G. Shiu, *JCAP* **1**, 2 (2007), arXiv:hep-th/0605045.
- [55] R. Holman and A. J. Tolley, *JCAP* **5**, 1 (2008), 0710.1302.
- [56] P. D. Meerburg, J. P. van der Schaar, and P. Stefano Corasaniti, *JCAP* **5**, 18 (2009), 0901.4044.
- [57] F. Schmidt and M. Kamionkowski, *Phys. Rev. D* **82**, 103002 (2010), 1008.0638.
- [58] D. Babich, P. Creminelli, and M. Zaldarriaga, *JCAP* **8**, 9 (2004), arXiv:astro-ph/0405356.
- [59] J. Fergusson and E. S. Shellard, *ArXiv e-prints* (2011), 1105.2791.
- [60] R. Scoccimarro, *MNRAS* **299**, 1097 (1998), arXiv:astro-ph/9711187.
- [61] M. Crocce, S. Pueblas, and R. Scoccimarro, *MNRAS* **373**, 369 (2006), arXiv:astro-ph/0606505.
- [62] V. Springel, N. Yoshida, and S. D. M. White, *New Astronomy* **6**, 79 (2001), arXiv:astro-ph/0003162.
- [63] V. Springel, *MNRAS* **364**, 1105 (2005), arXiv:astro-ph/0505010.
- [64] S. D. M. White, *ArXiv Astrophysics e-prints* (1994), arXiv:astro-ph/9410043.
- [65] S. H. Hansen, O. Agertz, M. Joyce, J. Stadel, B. Moore, and D. Potter, *Astrophys. J.* **656**, 631 (2007), arXiv:astro-ph/0606148.
- [66] D. Jeong, dissertation (2010), URL http://www.pha.jhu.edu/~djeong/dissertation/djeong_diss.pdf.
- [67] E. Sirko, *Astrophys. J.* **634**, 728 (2005), arXiv:astro-ph/0503106.
- [68] D. J. Price, *Publications of the Astronomical Society of Australia* **24**, 159 (2007), 0709.0832.